SPACE APPLICATIONS INSTITUTE

ON THE RETRIEVAL ACCURACY OF THE ALBEDO AND BRF FIELDS: POTENTIAL OF THE LSPIM/PRISM-SENSOR

by
Peter Vogt, Michel M. Verstraete, Bernard Pinty,
Massimo Menenti, Augusto Caramagno, Michael Rast

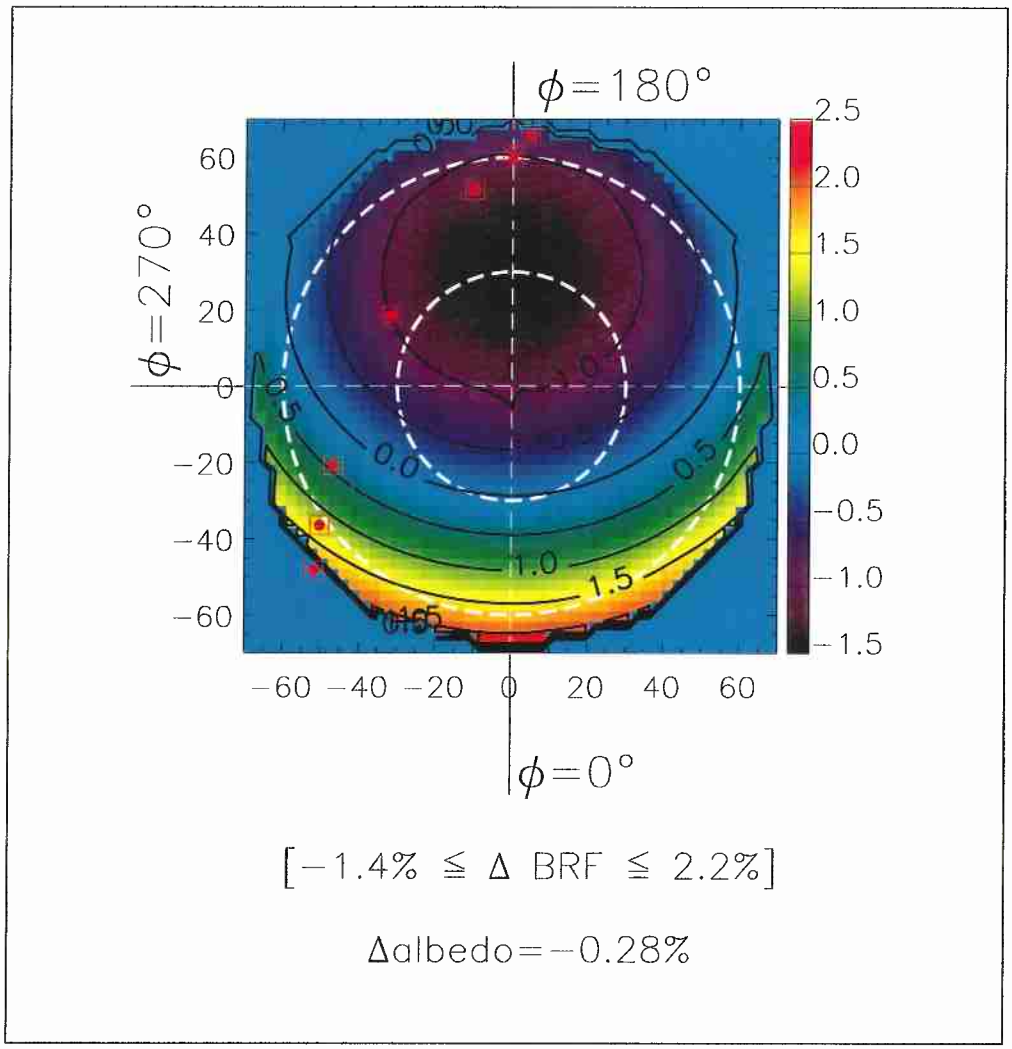

JOINT RESEARCH CENTRE
EUROPEAN COMMISSION

EUR 19016 EN

1999

Caption: Retrieval accuracy in percent of the BRF field and the hemispherical albedo in the RED spectrum derived from directional BRF measurements (red squared dot) for a simulated orbit of the PRISM sensor. The surface type is Steppe with a solar zenith angle of $\theta_0 = 45°$ (cross). The black iso-lines refer to the the BRF retrieval error distribution with a step size of $\Delta 0.5\%$. The white dashed circles indicate the observer zenith angle at 30° and 60°. The minimum and maximum BRF deviation is given in brackets. These results are based on an analysis of noisy data, as described on page 6.

SPACE APPLICATIONS INSTITUTE

ON THE RETRIEVAL ACCURACY OF THE ALBEDO AND BRF FIELDS: POTENTIAL OF THE LSPIM/PRISM-SENSOR

Peter Vogt*
Michel M. Verstraete
Bernard Pinty
Space Applications Institute
EC Joint Research Centre, TP 440
I-21020 Ispra (VA), Italy

Massimo Menenti
Université Louis Pasteur
LSIIT/GRTR
F-67400 Illkirch, France

Augusto Caramagno
GMV
C/Isaac Newton 11, Tres Cantos
S-28760 Madrid, Spain

Michael Rast
European Space Research and Technology Centre (ESTEC)
European Space Agency (ESA), Keplerlaan, 1, Postbus 299
NL-2200 AG Noordwijk, The Netherlands

* On leave from: Raytheon ITSS, 4400 Forbes Blvd., Lanham, MD, 20706-4392 USA.

EUR 19016 EN

JOINT RESEARCH CENTRE
EUROPEAN COMMISSION

1999

LEGAL NOTICE

EUR 19016 EN

Printed in Italy

Abstract

This report investigates some aspects of the information contained in directional measurements as may be provided by the PRISM sensor of ESA's Land-Surface Processes and Interactions Mission. Specifically, the goal is to assess the retrieval accuracy with which the albedo and the bidirectional reflectance factor (BRF) field can be retrieved as a function of the number of observations and their angular distribution. A BRF data base is generated for different surface types, solar positions, and wavelengths. These BRFs are artificially contaminated with a realistic amount of noise in order to approximate actual measurement conditions. A parametric BRF model is inverted against these noisy data to retrieve the model parameters describing the anisotropy of the reflectance field. The model is then run in a forward mode with these retrieved parameters to reconstruct the entire BRF field and to estimate the albedo values. Finally, the retrieval accuracy for both the BRF field and the albedo is estimated by comparing the original and the reconstructed values and fields. A sensitivity study is performed with respect to the number of available observations and their angular distribution. In the case of a single observation, the retrieval accuracy based on the assumption of a Lambertian surface reflectance is compared to the one based on the assumption of a typical BRF field. The capability of the PRISM sampling strategy to usefully sample the variance of the top-of-atmosphere BRF field is investigated by simulating different atmospheric conditions over the measured surface BRF field of an Aspen forest.

Keywords: Multi-angular measurements, BRDF, albedo.

Contents

List of Figures

List of Symbols

Roman Symbols

Symbol	Dimension	Description
b_M	[-]	MRPV model parameter
k	[-]	MRPV model parameter
g	[rad]	phase angle
G	[-]	geometry factor in the MRPV model
H	[-]	hotspot factor in the MRPV model

Greek Symbols

Symbol	Dimension	Description
δ	[-]	aerosol optical depth
λ	[nm]	wavelength
ϕ	[rad]	relative azimuth angle
ρ_0^M	[-]	MRPV model parameter
ρ_s^M	[-]	measured/modeled BRF
$\overline{\rho}$	[-]	average measured BRF
σ	[-]	standard deviation of the Gauss distribution
θ_0	[rad]	solar co-elevation angle
θ	[rad]	observer co-elevation angle

List of Acronyms

BRF	Bidirectional Reflectance Factor
BRDF	Bidirectional Reflectance Distribution Function
f_{APAR}	fraction of Absorbed Photosynthetically Active Radiation
LADF	Leaf Angle Distribution Function
LAI	Leaf Area Index
LSPIM	Land-Surface Processes and Interactions Mission
MISR	Multi-angle Imaging Spectro-Radiometer
MRPV	Martonchik modified Rahman Pinty Verstraete radiative transfer model
NIR	Spectral band in the Near-infrared spectrum
POLDER	POLarization and Directionality of Earth Reflectances
PRISM	Processes Research by an Imaging Space Mission
RED	Spectral band in the red spectrum
TOA	Top of Atmosphere

Chapter 1

Introduction

Spectral radiances scattered by the Earth system and measured by means of space-borne sensors are affected by many processes and variables. These include the state of the atmosphere (e.g., water vapor and aerosols), meteorological conditions (e.g., cloud cover, temperature, wind), radiative properties of the surface (e.g., spatial, spectral, chemical, and biophysical conditions), and the illumination/observation geometry. The Bidirectional Reflectance Distribution Function (BRDF) is a statistical description of the reflectance of a surface, for any given direction of illumination and observation. Since both sources of light and detection are always of finite dimensions, it is not possible to measure the BRDF directly. Instead, such measurements are called bi-conical. In practice, they are often normalized by the reflectance of a Lambertian panel, illuminated and observed under identical conditions. This normalized value is called the Bidirectional Reflectance Factor (BRF), although this is an abuse of language.

The albedo is defined as the ratio of the reflected to the incident solar flux at a surface. It is a measure of the fractional amount of solar radiation absorbed by the surface and linked to such important parameters as the biomass and the net primary production. The spectral albedo for a certain solar position is obtained by integrating the BRF field over the upper hemisphere (Nicodemus[7]):

$$\alpha(\theta_0, \lambda) = \frac{1}{\pi} \int_0^1 \int_0^{\pi/2} \rho(\theta_0, \theta, \phi, \lambda)\, \mu\, d\mu\, d\phi \tag{1.1}$$

where λ is the wavelength, θ_0 and θ are the solar and observer zenith angle (with $\mu = \cos\theta$), and ϕ is the relative azimuth between these directions.

In case the BRFs do not change with the geometry of observation the surface is called Lambertian. However, observations in the past 15 years have conclusively established that the Earth's surface is non-Lambertian or anisotropic (see, e.g., Kriebel[17][18][19], Kimes[12][16][15] [14][13], Deering[3][2], Irons[10][9]). Moreover, in 1985, Kimes and Sellers [16] demonstrated that neglecting BRF-effects result in spectral albedo errors of up to 40%.

In the past, directional variations in the measurements were often treated as a source of noise. By contrast, the present research is focused on exploiting the anisotropy of the reflectance field as a potential new information source to derive characteristic features of the target under investigation:

1. Surface
   An improved BRF sampling will lead to an increased accuracy in the reconstruction of BRF fields and, after hemispherical integration, in the estimation of the albedo. Over vegetated terrain, an improved assessment of the albedo can be used in climatological models for better estimates of photosynthesis, transpiration rates, and the amount of absorbed photosynthetically active radiation (f_{APAR}) (e.g., Clevers et al.[1], Sud and Molod[27], Sellers[24], Sellers et al.[25], Shuttleworth and Dickinson [26], von Schönermark et al.[31]). These parameters play an important role in the way the vegetation and the atmosphere interact.

   An improved BRF sampling permits more accurate estimates of surface attributes by inversion of BRF models. Angular signatures comprise an additional geometrical information content, which can improve the process of classifying and monitoring various vegetation specific characteristics (e.g., LAI, LADF, crown size, ground cover fraction: Pinty and Verstraete[22]; Kimes and Sellers[16]; Vogt[30]) and land cover classification (Gerstl[8]).

2. Atmosphere
   In order to minimize atmospheric perturbations on the surface BRFs, cloud-free conditions are required. Thin cirrus clouds at high altitudes, also referred to as sub-visual cirrus, affect the measured signal and are difficult to detect in satellite images. Here, the multi-angle viewing strategy might contribute to a better cloud detection since large off-nadir zenith angles accentuate the effect of thin clouds due to the increased optical path length in the atmosphere. Contrariwise, this cloud type is usually difficult to detect with nadir measurements alone. Furthermore, the measurement of more scattering angles will contribute to a better description of the atmospheric scattering phase function and the aerosol size distribution (Vermote[28]; Martonchik et al.[21], Kahn et al.[11], Diner et al.[5][4]; Leroy et al.[20]). The combination of a more accurate cloud detection with a better description of the atmospheric state will reduce the atmospherically introduced uncertainties on the signal and result in an improved retrieval of both atmospheric and surface properties.

New sensors (e.g., MISR, ATSR, POLDER) with different angular sampling strategies have been designed. They address the interaction between the BRF field and several environmental parameters in the Earth atmosphere system. The concept of the Land-Surface Processes and Interac-

tions Mission (LSPIM[23]) of the European Space Agency (ESA) capitalizes on recent findings and will permit to accommodate the increasingly demanding requirements of the scientific community. The payload is an imaging spectrometer (PRISM: Processes Research by an Imaging Space Mission) covering the region 450 to 2350 nm with two additional channels in the thermal infrared ($8.0 - 8.5\mu$m; $8.6 - 9.1\mu$m). The nominal directions of observation of the PRISM instrument are $0°, \pm 45°, \pm 60°, \pm 70°$ in the along track direction forward (positive) and backward (negative) of the nadir. In addition, in the current proposed design, the first off-nadir angle of observation is user-selectable in the range 25 to 45°, to obtain a measurement as close as possible to the hot spot condition. The latter is a local reflectance maximum resulting from the absence of shadows when viewing in the retrosolar position. The sensor also allows for user-selected directional sampling in both along- and across-track directions. This feature can be used to study the impact of different sampling strategies on the retrieval accuracy of geophysical parameters. Future research may result in an angular sampling, optimized after launch to address specific issues.
The goal of this report is to determine the qualitative and quantitative impact on the estimation of the albedo and the BRF field resulting from

1. a variable number of observations for two given solar zenith angles,
2. the assumption of a Lambertian surface reflectance versus a predefined BRDF shape in the case of single arbitrarily directed observation.

In the next chapter, a parametric BRF model is introduced, which is capable to reconstruct an entire BRF field from a limited number of measured or simulated BRFs. In section 2.4 a sensitivity study is performed with respect to the above mentioned two topics and an estimate of the impact of different atmospheric states on the top of atmosphere (TOA) reflectance field is provided. The focus of the latter is to examine the PRISM directions of observations for an adequate description of the TOA reflectance field, which, in turn, is the stringent stipulation for a precise determination of the surface BRF field and the albedo. For the purpose of this study, all simulations in the two spectral bands RED and NIR have been performed monochromatically at 670 nm and 870 nm respectively.

Chapter 2

Simulation strategy

2.1 Model description

The Martonchik modified Rahman Pinty Verstraete radiative transfer model (MRPV, Engelsen et al. [6]) is a parametric BRF model, which simulates the BRDF of an arbitrary surface by means of three parameters ρ_0^M, b_M, k:

$$\rho_s^M(\theta_0, \theta, \phi; b_M, k) = \rho_0^M M(\theta_0, \theta, k) F_M(g; b_M) H(\overline{\rho}, G) \tag{2.1}$$

where:

$$M(\theta_0, \theta, k) = [(\cos\theta_0 \cos\theta)/(\cos\theta_0 + \cos\theta)]^{k-1} \tag{2.2}$$

$$F_M(g; b_M) = \exp(-b_M \cos g) \tag{2.3}$$

$$H(\overline{\rho}, G) = 1 + \frac{1 - \overline{\rho}}{1 + G} \tag{2.4}$$

$$G = [\tan^2\theta_0 + \tan^2\theta - 2\tan\theta_0 \tan\theta \cos\phi]^{0.5} \tag{2.5}$$

$$\cos g = \cos\theta_0 \cos\theta + \sin\theta_0 \sin\theta \cos\phi \tag{2.6}$$

where, ρ_s^M is the BRF at the angular position (θ_0, θ, ϕ), ρ_0^M describes the overall reflectance magnitude, k the steepness of the bowl shape of the BRDF, and b_M the forward/backward asymmetry factor of the anisotropy function $F_M(g; b_M)$. The hotspot correction factor $H(\overline{\rho}, G)$ permits a limited parameterization of the hot spot feature without requiring an additional model parameter. Here, $\overline{\rho}$ is the average reflectance factor of the BRF field and G is a geometry factor. Finally, g is the scattering angle between the directions of observation and illumination, a quantity which depends on the zenith (θ_0 and θ) and the relative azimuth (ϕ) angles.

The MRPV model can be used to

a) generate BRF fields using predefined values for ρ_0^M, b_M, k;

b) retrieve the 3 model parameters by inversion against a limited data set with a minimum of 3 BRFs;

c) estimate the albedo by hemispherical integration over the observation directions.

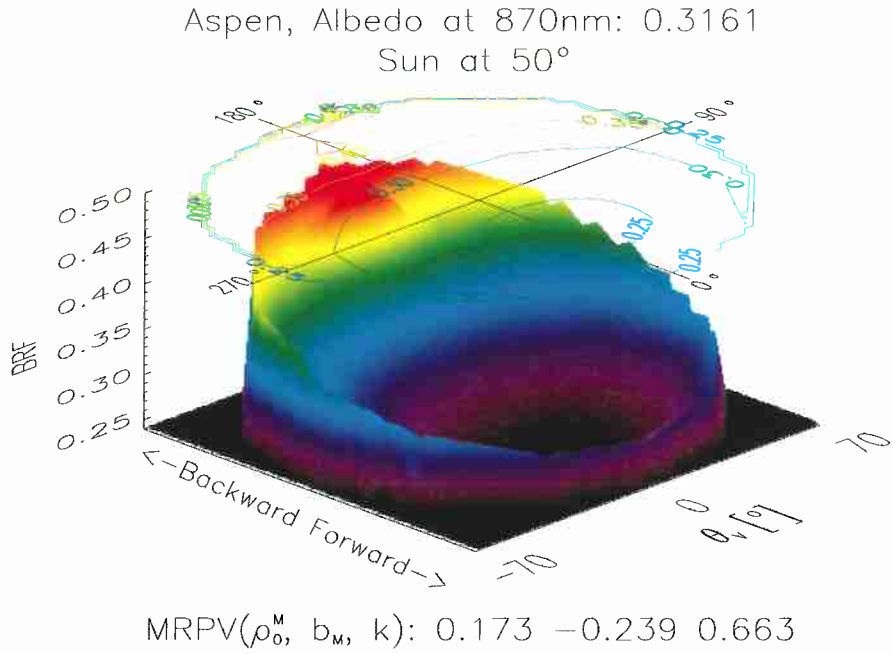

Figure 2.1: Simulated near-infrared BRF field using the optimal MRPV model parameters retrieved from measured BRFs over an Aspen forest by Deering [2]. The MRPV parameter ρ_0^M describes the overall reflectance magnitude, b_M the forward/backward asymmetry, and k the steepness of the bowl shape of the BRDF.

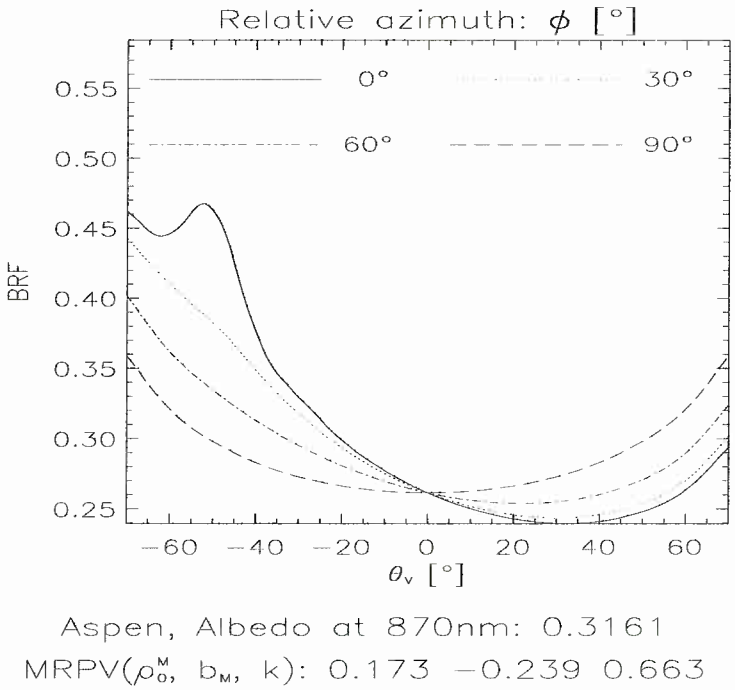

Figure 2.2: BRF for Aspen forest along several relative azimuthal planes (see figure 2.1).

The MRPV model has been successfully used to reconstruct the BRF field out of a limited number of synthetic or measured data (Engelsen et al.[6]). A typical example of the anisotropic reflectance behavior of a natural target is shown in figure 2.1. Another way to illustrate the shape of the BRF field is to depict the BRF values along the plane formed by the direction of illumination and the local vertical (principal plane). In addition to the overall bowl shape of the BRF field, specific features appear mostly along the principal plane. They include the higher reflectivity in the backward scattering region and the hotspot. By convention, the principal plane therefore corresponds to relative azimuth directions $\phi = [0°, 180°]$ (see figure 2.1). Figure 2.2 exhibits reflectance variations along several azimuthal sections through the BRF field of figure 2.1.

2.2 Simulated BRF data set

Engelsen et al.[6] provide the values of the MRPV model parameters ρ_0^M, b_M, k for a wide variety of surface types for which measurements or realistic simulations existed. The values of the model parameters were obtained by inverting the MRPV model against a discrete number of measurements for different targets. The same model can then be invoked in a forward mode to calculate the complete BRF fields for the geophysical conditions of table 2.1.

observer zenith angle [°]	$[0, 10, 20, 30, 40, 50, 60, 70]$
relative azimuth angle [°]	$[0, 30, 60, 90, 120, 150, 180]$
solar zenith angle [°]	$[20, 50]$
surface type	aspen, spruce, pine,
	tropical forest, corn, grassland,
	hard wheat, soil, steppe
wavelength [nm]	$[670, 870]$

Table 2.1: Geophysical conditions used in the albedo retrieval accuracy study.

In addition, the spectral albedo is calculated from each surface BRF field for the two solar positions $\theta_0 = 20°, 50°$ resulting in 36 albedos (9 surface types, 2 wavelengths, and 2 solar zenith angles: $9 \times 2 \times 2 = 36$).

The assessment of the retrieval performance is now investigated under realistic measurement conditions by applying a normalized Gaussian-distributed noise with a standard deviation of $\sigma = 0.05$ to each simulated BRF (figure 2.3). As a result, the noise contaminated BRF is, with a probability of 66%, within $\pm 5\%$ of the corresponding true BRF. In order to avoid unrealistically noisy BRFs (outliers), a maximum deviation of $\pm 20\% \equiv \pm 4\sigma$ of the nominal value of the true BRF is permitted. Noisy BRFs exceeding this threshold are discarded and regenerated until they are within the allowed threshold range.

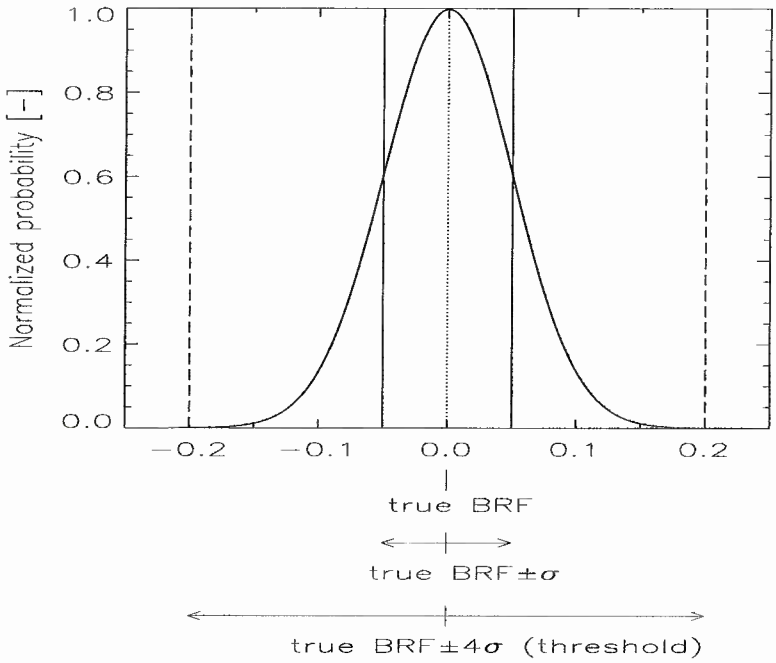

Figure 2.3: Application of Gaussian distributed noise on the simulated BRFs. The vertical lines indicate the true BRF (dot), the standard deviation range σ (solid), and the threshold range 4σ (dashed).

2.3 Orbit simulations

As part of the technological phase A study of LSPIM, a mission simulator (MOSAP-L) has been developed by GMV S.A., Madrid, Spain, to address the directional sampling capability and the orbital characteristics of the platform embarking the PRISM sensor. The LSPIM mission is planned from the outset in conjunction with an ambitious network of field sites, which provides at once a critical mass of investigators and users of PRISM data, and a mechanism to evaluate the performance of the algorithms proposed for the analysis of such data. A global map of test sites covering a wide variety of biome types has been set up. As an example, the IMGRASS test site (Latitude: $44.045N$, Longitude: $116.367E$) in the People's Republic of China has been selected to perform a sensitivity study on the BRF field retrieval accuracy with respect to the number of observations and their position in the angular space. Figure 2.4 shows the GMV simulated orbits over the IMGRASS test site for the 15-29 of March. Each BRF sequence contains 37 samples, one every 10 seconds, starting with the southern-most squared-dot. The corresponding solar positions are marked with 37 red dots for each orbital sequence. The annotated number at the southern-most squared-dot is the sequence number within a cycle. The squared-dots show the nominal PRISM directions of observa-

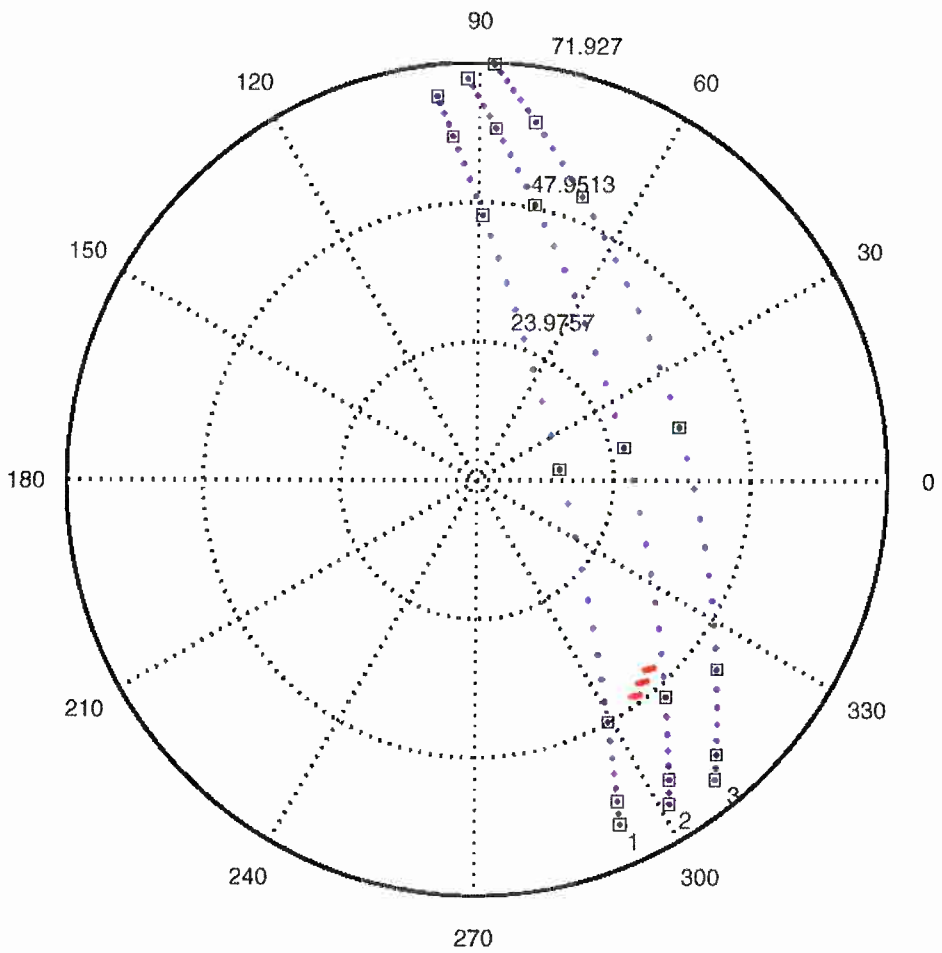

Figure 2.4: GMV simulated orbits over the IMGRASS test site for the period 15-29 of March. Given the nominal parameters of the orbit of the platform, the selected site can be observed on three occasions during this period. The blue dots indicate the possible sampling positions of the PRISM sensor and the red dots the corresponding solar position for each of the three orbital sequences. Squared blue dots refer to the nominal directions of observation in the current design.

tion. The dots in-between indicate samples that the sensor might be able to take, but before the platform is again stable in the new angular position at the nominal PRISM angle. The actual measurement conditions for the PRISM sensor will usually not include an exact nadir measurement (see figure 2.4). For the purpose of this assessment, observation conditions corresponding to orbit number 3 have been selected, as they provide a sort of 'worst case scenario'. The corresponding averaged solar zenith angle is $\theta_0 = 45°$. The BRF field for the IMGRASS test site is simulated by assuming a surface of type Steppe with the corresponding 3 model parameters of the MRPV model. BRFs are calculated for the observer

zenith angles $0°, 10°, 20°, ..., 70°$, relative azimuth $0°, 30°, 60°, ..., 180°$, and the solar position $\theta_0 = 45°$. Hereafter, this BRF matrix will be referred to as the true BRF matrix.

2.4 Sensitivity case study

The BRF field as sampled by the IMGRASS test site matrix as well as those corresponding to the matrices of the targets outlined in table 2.1 are integrated to obtain the true albedo. Since the retrieval performance must be investigated under realistic measurement conditions, noise contaminated BRFs are generated by the application of a 5% Gaussian-distributed noise to each reflectance factor. The values for the noisy albedo are calculated by hemispherical integration of these noisy BRF fields. The accuracy of these estimations is assessed by comparison with the albedo and the BRF field of the corresponding 'true' data base. Here, the retrieval accuracy for both albedo and BRF field is dependent on the number of available observations and their angular distribution. In this sensitivity study, a limited number of BRFs is extracted from the noisy BRF matrix. In conjunction with the known solar position, they are used to invert the MRPV model to obtain the three model parameters (ρ_0^M, b_M, k). Applying the derived values of these model parameters in a forward mode leads to the reconstruction of the entire BRF field. The latter is integrated to estimate the noisy albedo and is compared to the true albedo, which is based on all 50 directions of observation (7 off-nadir observations, 7 relative azimuths, and the nadir observation: $7 \times 7 + 1 = 50$). The quality of the retrieval is expressed as the relative difference in percent of the retrieved versus the simulated BRF/albedo, normalized by the simulated BRF/albedo.

The sensitivity investigation is articulated around 12 cases, which are depicted in figures 2.5 (page 10) and 2.6 (page 11). They are characterized by either a progressive decrease in the number of observations, or, when the number of observations is the same, a change in their location in angular space. The latter permits to investigate the retrieval accuracy as a function of angular position when the number of observations is fixed. For example, we have the nadir observation and 1 observation close to nadir. The retrieval accuracy can be expected to be almost the same as when we use the nadir observation alone since the 2 observations are taken at approximately the same angular position. By opposition, the retrieval accuracy when using the nadir and an off-nadir observation at, e.g., $\theta = 60°$ is expected to increase since we obtain more information on the anisotropy of the BRF field.

Case 1: 50 observations

All 50 observations (7 off-nadir observations, 7 relative azimuths, and the nadir observation: $7 \times 7 + 1 = 50$) are used for the calculation of the

albedo. Please note that due to the azimuthal symmetry of the model with respect to the principal plane the BRFs for the 7 off-nadir observations with the relative azimuth angle $\phi = 90°$ are identical to the ones with the relative azimuth angle $\phi = 270°$. The same holds true for the off-nadir observations at $\phi = 30°$ and $\phi = 330°$, etc. (see figure 2.5).

Case 2: 22 observations
The nadir observation and the directions of observation of the 3 nominal off-nadir PRISM angles are selected along the seven azimuthal planes ($\phi = [0°, 30°, \ldots, 150°, 180°]$) resulting in 22 observations.

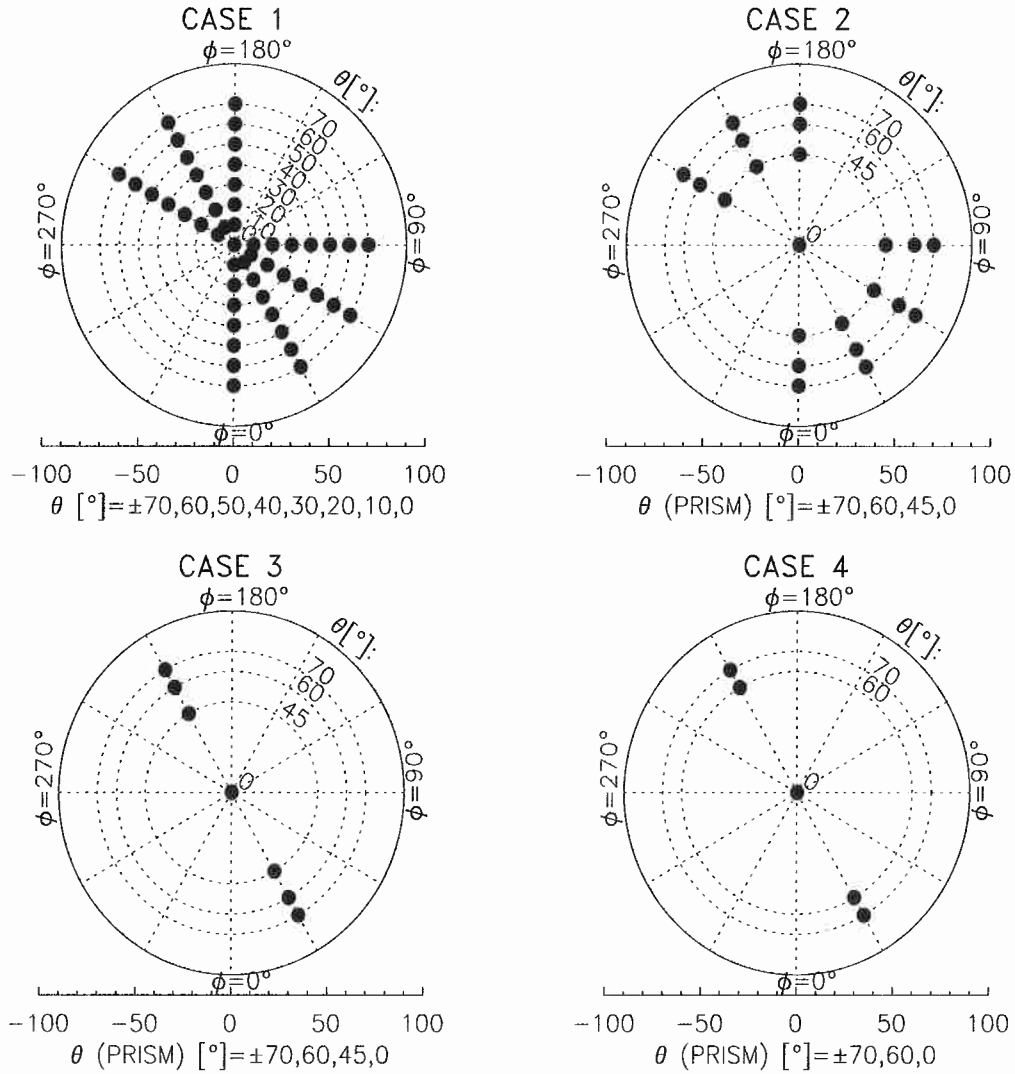

Figure 2.5: Definition of Cases 1 to 4 for the sensitivity study on the hemispherical albedo. The large dots denote the selected directions of observation.

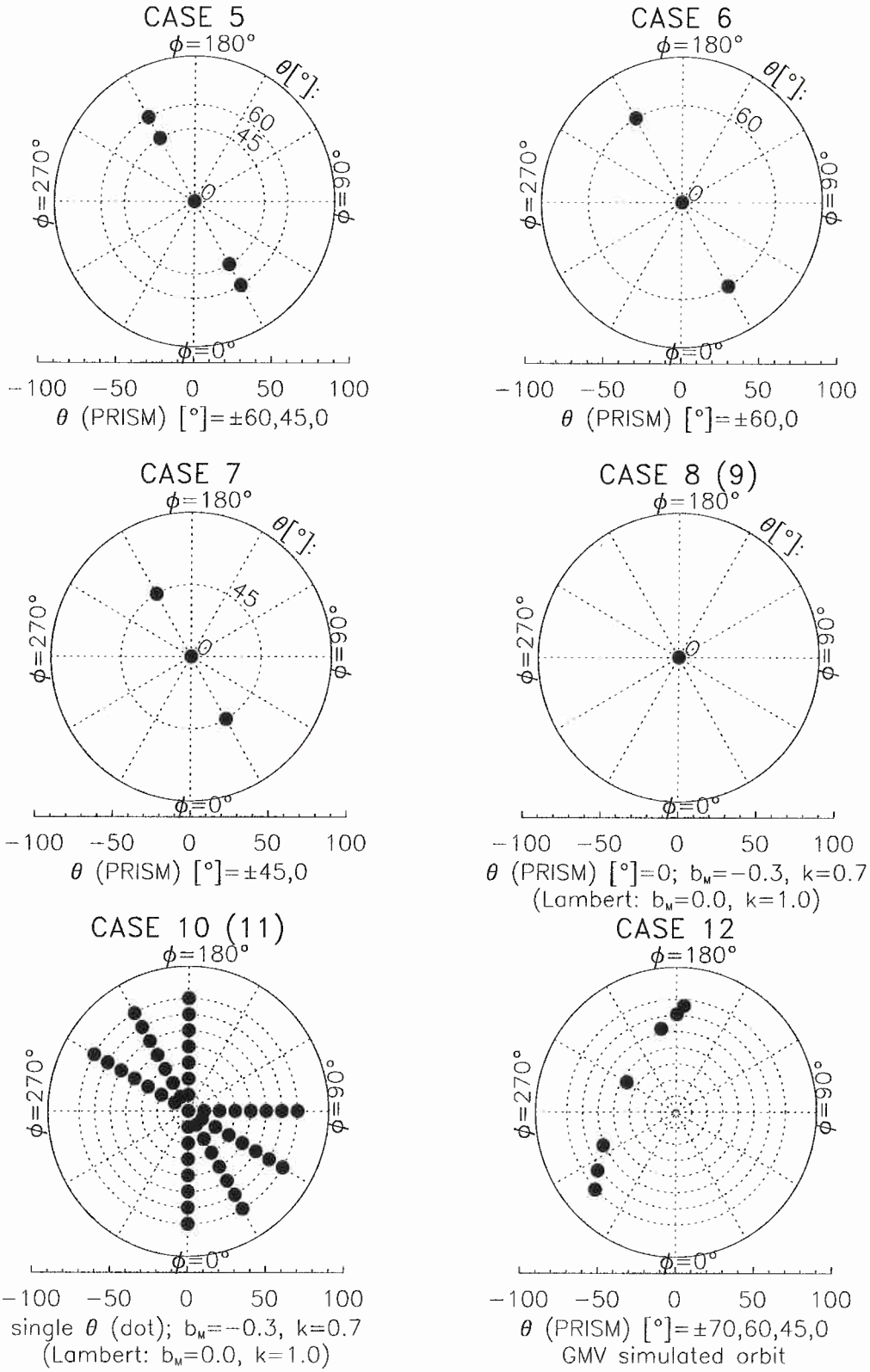

Figure 2.6: Same as figure 2.5 for Cases 5 to 12.

Case 3: 7 observations
The directions of observation of the 7 nominal PRISM angles in the plane $\phi = [30°, 210°]$ are selected. This plane is considered a reasonable compromise between the strong anisotropy along the principal plane and the less pronounced anisotropy along the cross plane ($\phi = [90°, 270°]$). In reality, neither the principal nor the cross plane will be encountered from the satellite, since the measurement sequence follows a curved path (see figure 2.4 on page 8). For the theoretical purpose of this exercise it is therefore sufficient to select the plane $\phi = [30°, 210°]$.

Case 4: 5 observations
The 5 PRISM angles $\theta = [0°, \pm 60°, \pm 70°]$ in the plane $\phi = [30°, 210°]$ are selected.

Case 5: 5 observations
The 5 PRISM angles $\theta = [0°, \pm 45°, \pm 60°]$ in the plane $\phi = [30°, 210°]$ are selected. Case 4 and Case 5 are characterized by the same number of observations but a different angular sampling. The purpose of these cases is to investigate the impact of different angular sampling of the BRF field on the albedo retrieval accuracy.

Case 6: 3 observations
The 3 PRISM angles $\theta = [0°, \pm 60°]$ in the plane $\phi = [30°, 210°]$ are selected.

Case 7: 3 observations
The 3 PRISM angles $\theta = [0°, \pm 45°]$ in the plane $\phi = [30°, 210°]$ are selected. A similar purpose as in Case 4/5 is pursued in Case 6 and Case 7 but with 3 observations only.

Case 8: 1 observation
The nadir observation is selected. No natural or man-made surface exhibits a perfect Lambertian reflectance. Consequently, the anisotropy of vegetated surfaces can, at a minimum, be crudely represented by the BRF field of a typical canopy. This is achieved by assigning the two MRPV model parameters b_M and k the fixed values $b_M = -0.3$ and $k = 0.7$ (Engelsen et al.[6] page 39, 41). In inverse mode, only the MRPV model parameter ρ_0^M, denoting the overall reflectance magnitude, needs to be derived. Following equation 2.1, the analytical expression for ρ_0^M reads:

$$\begin{aligned} \rho_0^M &= \exp\left[\ln \frac{\rho_s^M}{H(\overline{\rho}, G)} - \kappa + b_M \cos g\right] \quad \text{with} \\ \kappa &= (k-1)\ln\left[\cos\theta_0 \cos\theta(\cos\theta_0 + \cos\theta)\right] \end{aligned} \tag{2.7}$$

The measured BRF at the nadir position is assigned to ρ_s^M. Since we have only one measurement available, the average BRF $\overline{\rho}$ of the BRF field is

initially unknown and therefore approximated with $\overline{\rho} = \rho_s^M$ to be able to solve equation 2.7. The MRPV model is then invoked in forward mode with the parameter set (ρ_0^M, b_M, k) to reconstruct the entire BRF field. The average of the BRF field ($\overline{\rho}$) can now be determined and is re-entered in equation 2.7 to finally estimate ρ_0^M.

Case 9: 1 observation
The nadir observation is selected and a Lambertian surface reflectance is assumed. This is accomplished by setting $k = 1.0$, $b_M = 0.0$, and $\overline{\rho} = 1$ (equation 2.1).

Case 10: 1 observation
Case 10 is the generalization of Case 8 for single arbitrary selected directions of observations as indicated by the large dots in figure 2.6 (7 off-nadir angles: $\theta = \pm 10°, \pm 20°, \cdots, \pm 70°$, 7 relative azimuth angles: $\phi = 0°, 30°, \ldots, \pm 180°$ and the nadir observation: $7 \times 7 + 1 = 50 \times$ a single observation). Due to the assumed azimuthal symmetry of the BRF field with respect to the principal plane this sampling is sufficient to characterize the entire field.

Case 11: 1 observation
Case 11 is the generalization of Case 9 for single arbitrarily selected directions of observations as outlined for Case 10. A Lambertian BRF field is assumed.

Case 12: 7 observations
The directions of observation of the 7 PRISM angles were selected by GMV, Madrid, Spain for an orbit simulation over the IMGRASS test site.

The purpose of the Cases 8, 9 and Cases 10, 11 is to directly compare the albedo retrieval accuracy under the assumption of a Lambertian surface reflectance or a typical BRF field. The background of this comparison is based on the following thought experiment. Compared to operational sensors with a large total field of view, e.g., AVHRR, the PRISM sensor will gather data over a relatively small area, such that an approximately constant solar zenith angle for all pixels of the image can be assumed. Furthermore, we presume that each pixel exhibits the same surface type. This stipulation may be met for some satellite scenes of the test sites for the validation campaign of the LSPIM mission. Under these conditions, each pixel shows the same BRF field and therefore the same albedo. However, the BRF for each pixel will be different since each pixel is observed under a different direction. Applying a BRF model to the pixel related BRF values will account for the anisotropy of the reflectance field and result in a constant albedo value for each pixel. By opposition, the assumption of a Lambertian surface for each pixel results in the BRF field instead of a con-

stant value within the satellite image. Using the Lambertian assumption therefore implies that the albedo is dependent on the observer geometry, a contradiction *per se*.

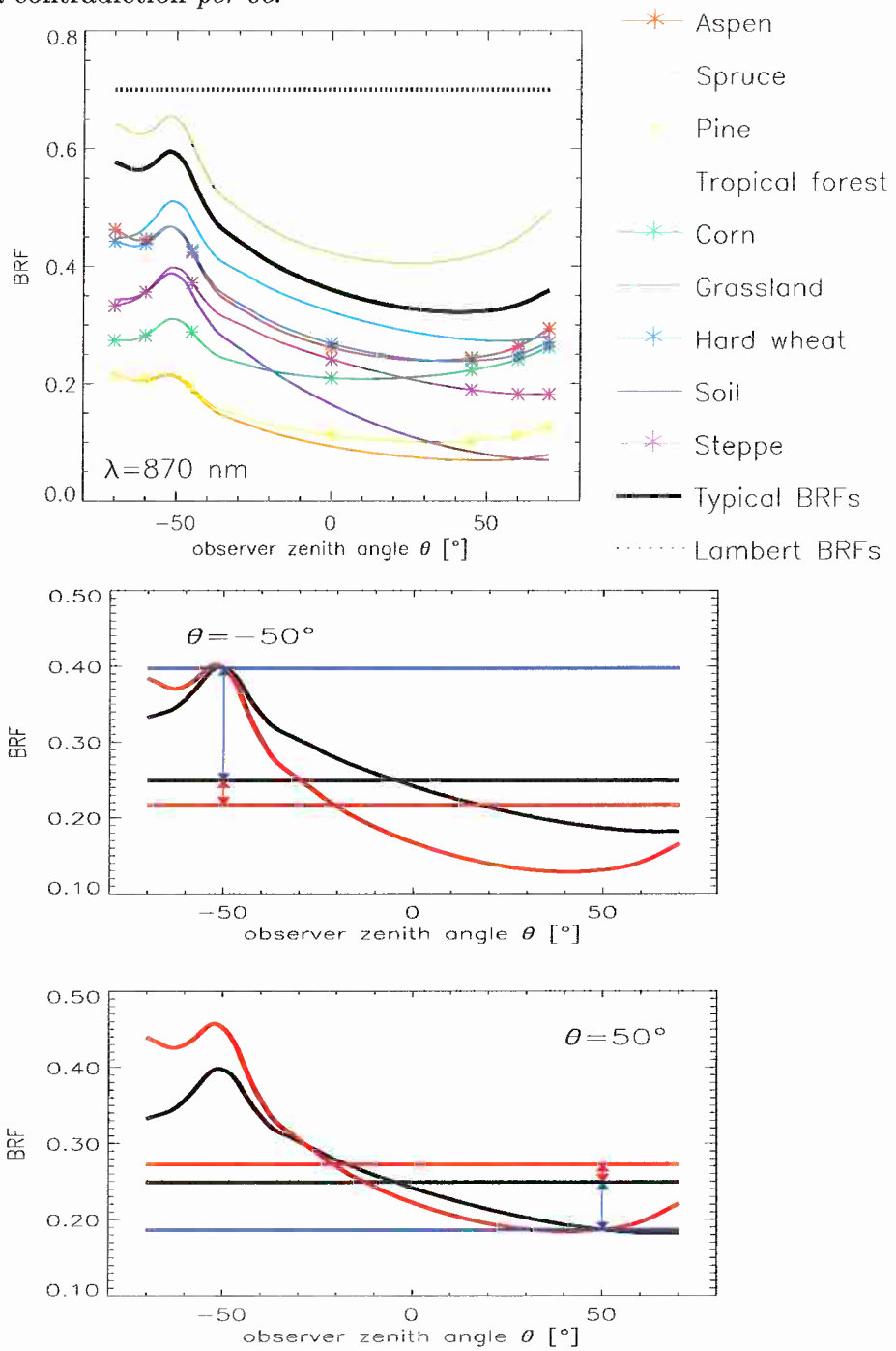

Figure 2.7: Top panel: BRF along the principal plane for all targets at $\theta_0 = 50°$. The BRF field of the typical or the Lambert BRFs is adjusted to the reflectance magnitude at the observer position $\Longrightarrow$ Middle and bottom panels: observer at $\theta = -50°$ and $\theta = 50°$ over Steppe: true BRF and albedo (black), typical (red: Case 8), Lambert (blue: Case 9), and albedo retrieval error (arrow).

In the case of 1 observation only (Case 8 to 11), the concept of the assumption of a typical BRF field or the Lambertian surface reflectance is depicted in figure 2.7. The colored lines in the upper part of the figure show the BRFs along the principal plane in the NIR spectral domain for all surface types outlined in table 2.1 and a solar zenith angle of $\theta_0 = 50°$. In addition, the black dotted, horizontal line denotes the BRFs for a Lambertian surface reflectance and the black solid line the BRFs for a typical BRF field. The albedo is assessed by vertically shifting the graph for the Lambertian or typical reflectance until it intersects with the measured reflectance value at the given observer position. This procedure is demonstrated in the lower part of the figure 2.7 over Steppe at the two observer positions $\theta = \pm 50°$. Here, the 3 different graphs denote the BRFs and the 3 horizontal lines the derived albedo. The color codes are, black for the true albedo and reflectance field, red for the assumption of the typical BRF field, and blue for the assumption of a Lambertian surface reflectance. Note that for the Lambert assumption the BRF field and the albedo coincide. Finally, the albedo retrieval error is annotated by vertical arrows in the corresponding color.

The cases 1 to 9 are used to assess the albedo retrieval accuracy (section 2.5) for the geophysical conditions outlined in table 2.1. Each case results in 1 albedo retrieval accuracy value for a given surface type and solar zenith angle. However, the cases 10 and 11 result in 50 albedo retrieval accuracy values, since each of the 50 different directions of observation is analyzed separately. In order to graphically display the retrieval results, the investigation of these cases is constrained to the IMGRASS test site with the surface type Steppe and the solar zenith angle $\theta_0 = 45°$. In section 2.6 the BRF field as well as the albedo retrieval accuracy is investigated by means of the cases 3, 8, 9, and 12 for the specifications of the IMGRASS test site. All investigations are performed in the RED and NIR spectral domains.

2.5 Albedo retrieval accuracy

The albedo retrieval accuracy for the Cases 1 through 9 is depicted in figure 2.8. For all surface types, solar zeniths, and wavelengths under investigation, the Cases 3 through 6 inclusively result in similar deviations from the true albedo of up to ±5%. The inclusion of more observations as in Case 2 and especially in Case 1 permits a better description of the BRF field and therefore the albedo. A decrease in retrieval performance is apparent for Case 7 with albedo retrieval errors of up to ±10%. Case 6 shows that a better description of the anisotropy of the surface reflectance field is obtained by preferentially selecting large observation zenith angles. This is coherent with *a priori* expectations as well as the results of our computations, which show that the fewer the observations and the more they resemble each other the more difficult it is to document the anisotropy

of the target and to estimate the albedo. A similar but less pronounced tendency is found for Case 4 and Case 5.

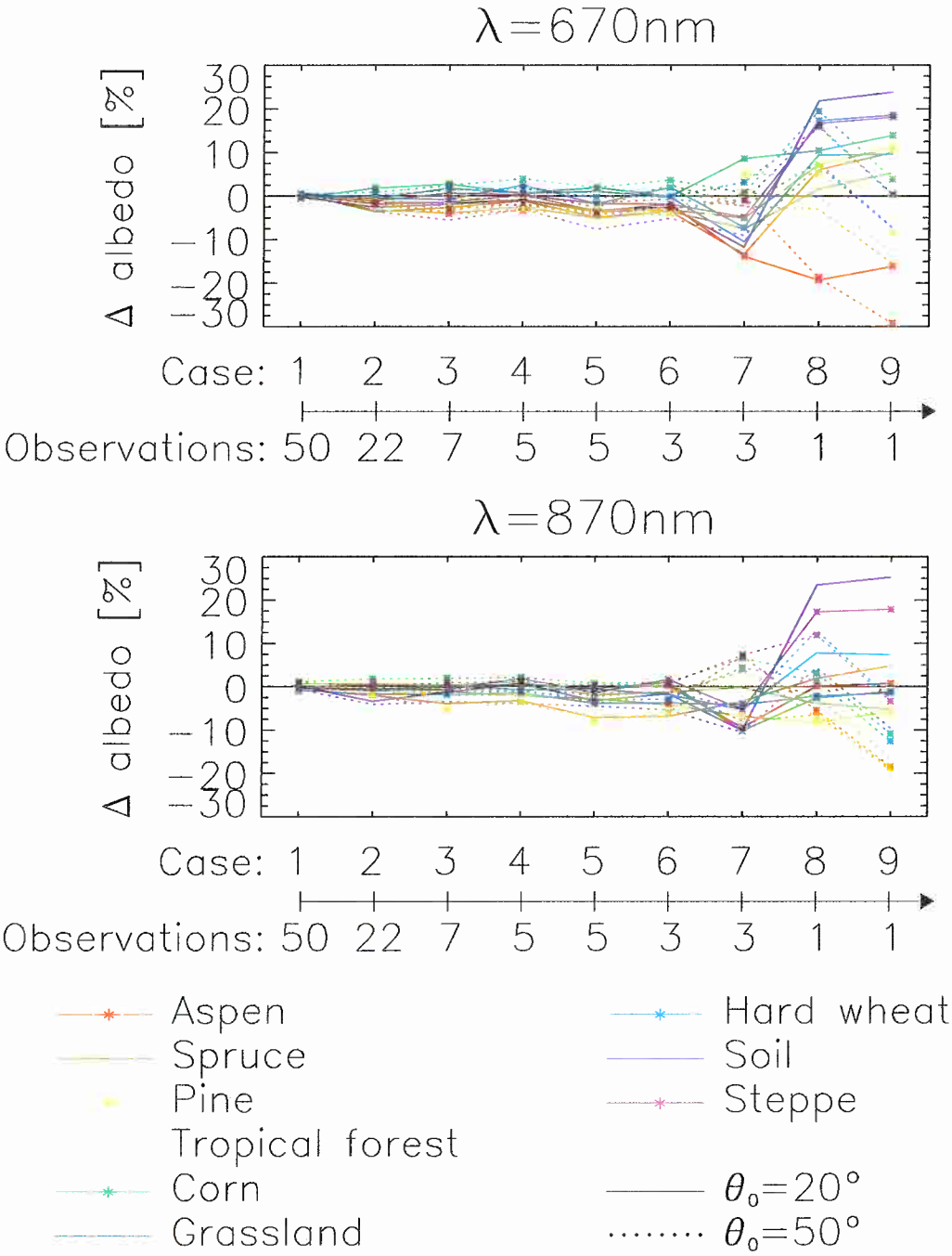

Figure 2.8: Relative error in albedo retrieval accuracy for Cases 1 to 9 over several surface types, for two solar positions $\theta_0 = 20°, 50°$, and in the RED (top) and NIR (bottom). These results are based on an analysis of noisy data, as described on page 6.

Comparing Cases 6 and 7 (with 3 observations) with Cases 4 and 5 (with 5 observations) shows that significant advantages can be derived even from a marginally higher number of observations (5 instead of 3), provided they sample relatively large zenith angles. The worst results, with an albedo retrieval error of up to ±25%, are obtained when only the nadir observation is used. Here, the predefined BRF field (Case 8) and the Lambertian assumption (Case 9) show a similar behavior.

The results for the retrieval accuracy of the albedo and, later on, the BRF field, are displayed in polar diagrams with the following notation:

- The black cross shows the solar position.
- Black iso-lines show the contour lines of the albedo retrieval error distribution, with a step size of $\Delta 10\%$.
- The white dashed circles indicate observation zenith angles at 30°, 60°.
- The red boxes with circles denote the positions at which the BRF values have been extracted from the noisy BRF field. These points therefore show the directions of observation which have been used for the retrieval performance.
- The relative azimuth is given outside of each image with a relative azimuth of $\phi = 180°$ denoting the backward scattering region, as can also be seen from the position of the sun (black cross).
- The upper image refers to the retrieval accuracy in the RED spectral band and the lower image in the NIR spectral band.
- For ease of comparison, all images of this sensitivity study are depicted within the same color scheme.
- The minimum and maximum relative errors are indicated in brackets. Throughout the figures 2.12 to 2.15, the simulated and the retrieved BRF field have been integrated to obtain the spectral albedo. The relative difference in spectral albedo, again normalized to the simulated spectral albedo, is outlined for each wavelength.

The deviation of the retrieved albedo from the 'true' constant albedo for Case 10 is shown in figure 2.9 on page 18. The assumption of a typical BRF field at arbitrary directions of observation leads to an albedo retrieval error of up to ±25%. By opposition, the assumption of a Lambertian reflectance field results in an albedo retrieval error between approximately −30% and +50% (figure 2.10 on page 19). Here, the direct assignment of the BRF measurement to the albedo leads to an overestimation in the backward scattering region and an underestimation in the forward scattering region (see also figure 2.7). Moreover, figure 2.10 permits an error assessment with respect to the observer geometry (red dots) when the Lambertian assumption is invoked. Here, the error range is dependent

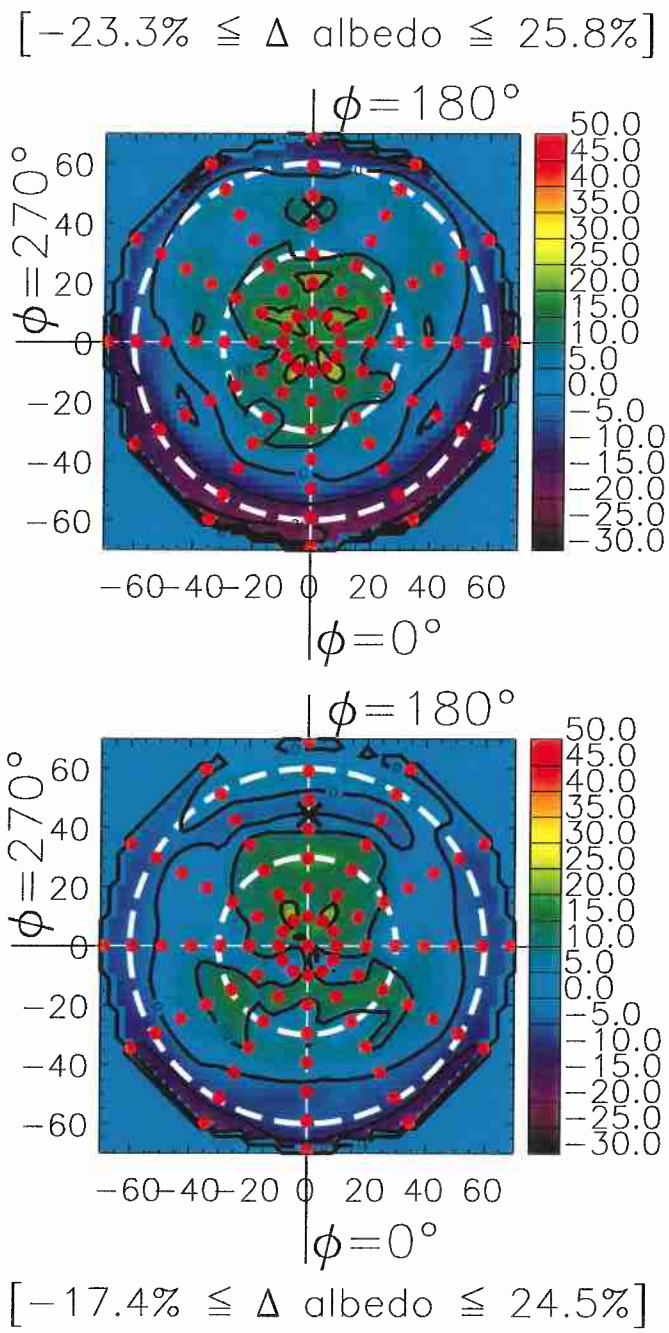

Figure 2.9: Case 10: Retrieval accuracy in percent of the hemispherical albedo derived from directional BRF measurement and assuming a typical BRDF shape using a single arbitrary direction of observation (red dot) over the IMGRASS test site in the RED (top) and NIR (bottom). The surface type is steppe with a solar zenith of $\theta_0 = 45°$ (cross), black iso-lines refer to the overlaid contour plot for the albedo retrieval error distribution with a step size of $\Delta 10\%$, white dashed circles indicate the zenith angle at 30° and 60°, and the minimum and maximum deviations are given in brackets. These results are based on an analysis of noisy data, as described on page 6.

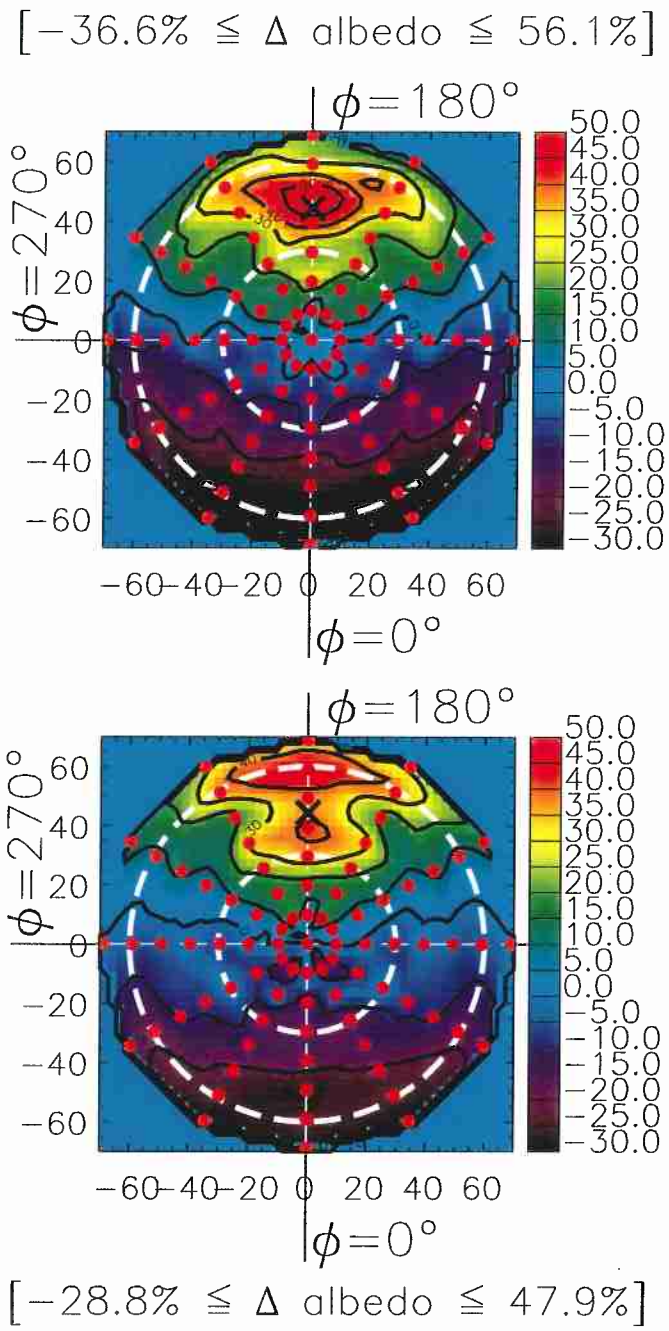

Figure 2.10: Case 11: Retrieval accuracy in percent of the hemispherical albedo derived from directional BRF measurement and assuming a Lambertian reflectance using a single arbitrary direction of observation (red dot) over the IMGRASS test site in the RED (top) and NIR (bottom). Further details as in figure 2.9.

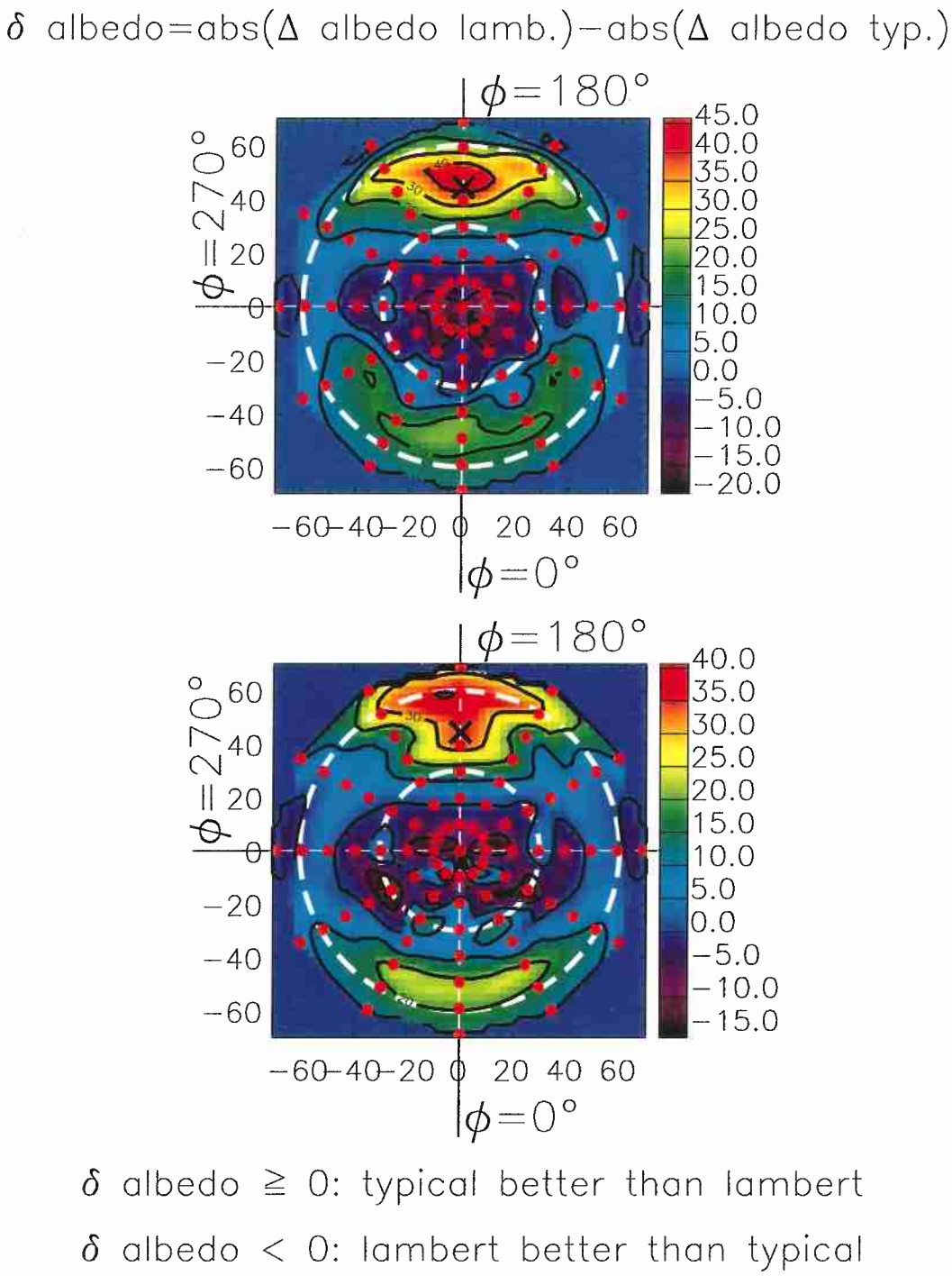

Figure 2.11: Difference between the albedo retrieval accuracy over Steppe derived from single directional BRF measurements assuming a Lambertian reflectance and the same variable estimate while assuming a typical BRF field. Positive (negative) values indicate a better performance of the assumption of a typical BRF field (Lambertian reflectance). Further details as in figure 2.9.

on the BRDF shape of the surface under study. For example, a smooth even surface, such as a sandy soil, would result in a more isotropic BRF field and therefore a reduced error range. However, most surface types are highly anisotropic and the biggest error will be found in the hot spot position since here the value for the albedo will be overestimated. This error increases with higher solar zenith angles due to the increasing contribution of the higher reflectance in the backward scattering region to the overall signal. Finally, figure 2.11 on page 20 exhibits the direct comparison between the assumption of a typical and a Lambertian BRF field. For this purpose, the difference in albedo retrieval (δ albedo) is defined as:

$$\delta\ albedo\ =\ |\Delta\ albedo\ Lambert|\ -\ |\Delta\ albedo\ typical| \tag{2.8}$$

Positive values of δ albedo indicate a better performance of the assumption of the typical BRF field while negative values favor the assumption of a Lambertian reflectance field. The results in figure 2.11 show a nadir centered elliptic region in which the Lambert assumption is superior to the assumption of the typical BRF field. The dimension of the ellipse are approximately $\theta = \pm 20°$ in the principal plane and $\theta = \pm 30°$ in the cross plane. Outside this region, the assumption of the typical BRF field results in an improved albedo retrieval, particularly in the forward and backward region of the principal plane where the anisotropy is most pronounced.

2.6 BRF field retrieval accuracy

The BRF field retrieval accuracy is investigated for Cases 3, 8, 9, and 12 for the IMGRASS test site. The corresponding figures 2.12 to 2.15 are displayed on the pages 22 to 25. The surface type is Steppe and the solar zenith angle $\theta_0 = 45°$.

Case 3:
For both spectral regions, the relative error for the BRF field was found to be less than approximately 4% and the albedo retrieval accuracy is within $\pm 1\%$ for the single noise distribution considered here. If this experiment were to be repeated for a large number of noise fields, one would expect the accuracy of the retrieved BRF field to be very close to the 5% noise applied initially.

Case 8:
The BRF retrieval accuracy covers an error range of 45% in the RED spectrum and 30% in the NIR spectrum. Case 8 represents an average shape of the BRF field and the retrieval accuracy is therefore dependent on the surface type. For example, if the predefined bowl-shape of the BRF field coincides with the BRDF of the surface under study, then the retrieval accuracy for the BRF field, and consequently the albedo, is expected to be similar.

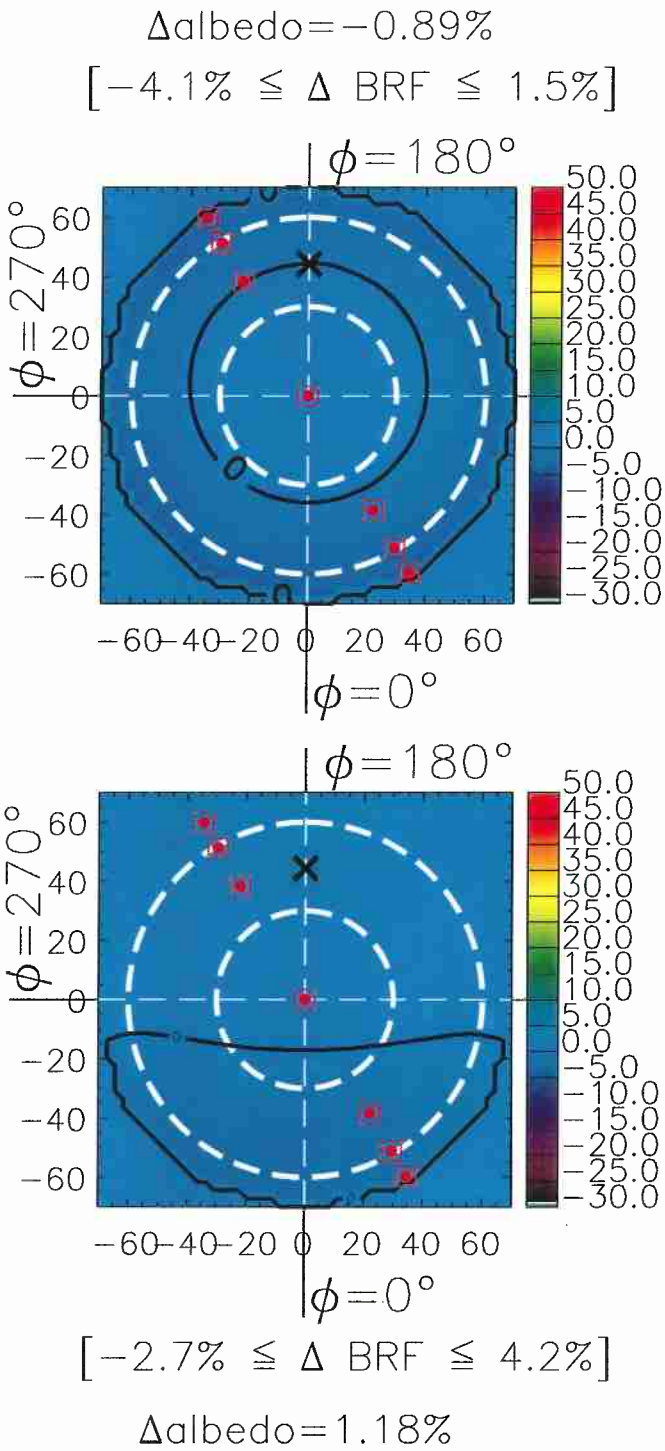

Figure 2.12: Case 3: Directional BRF and hemispherical albedo retrieval accuracy in percent when using all 7 directions of observation of the PRISM sensor in the red (top) and NIR (bottom). The surface type is Steppe with a solar zenith of $\theta_0 = 45°$ (cross), red square dots indicate the directions of observation, black iso-lines refer to the overlaid contour plot for the error distribution with a step size of $\Delta 10\%$, white dashed circles indicate the zenith angle at 30° and 60°, and the minimum and maximum deviations are given in brackets. These results are based on an analysis of noisy data, as described on page 6.

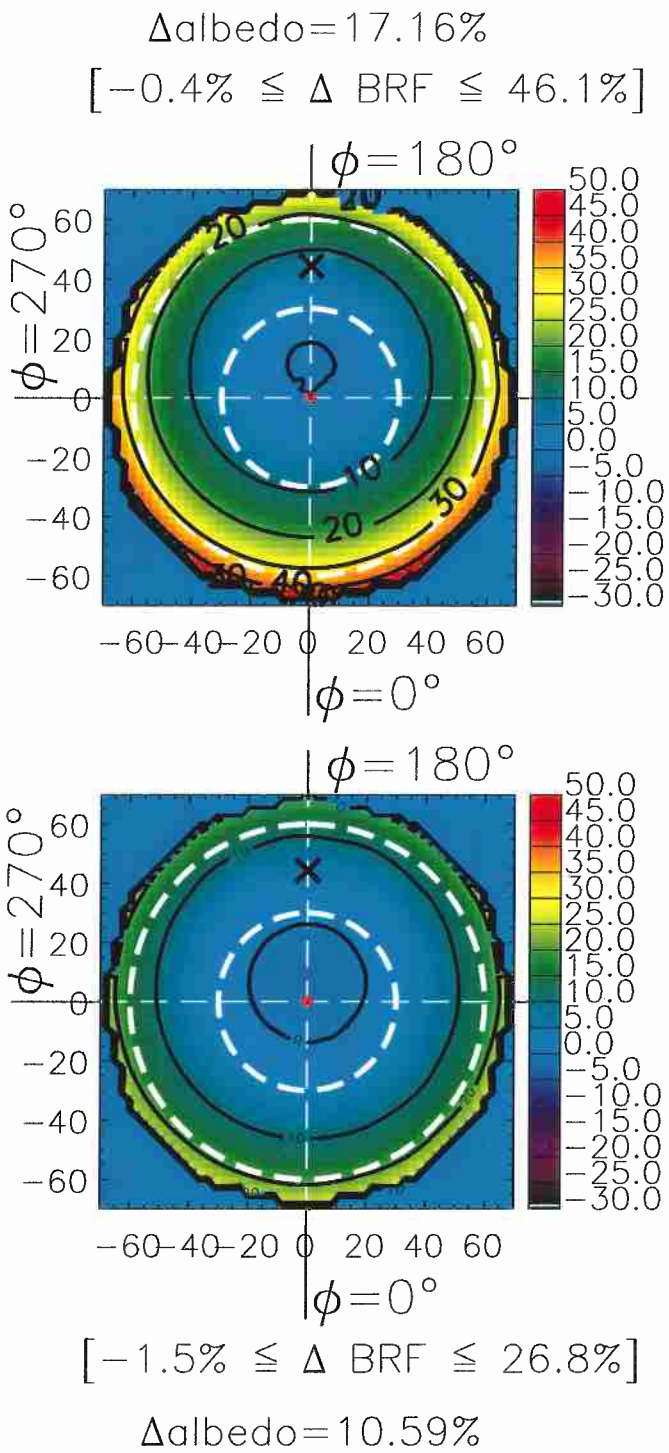

Figure 2.13: Case 8: Directional BRF and hemispherical albedo retrieval accuracy in percent when using the nadir observation only and a typical BRDF shape in the RED (top) and NIR (bottom). Further details as in figure 2.12

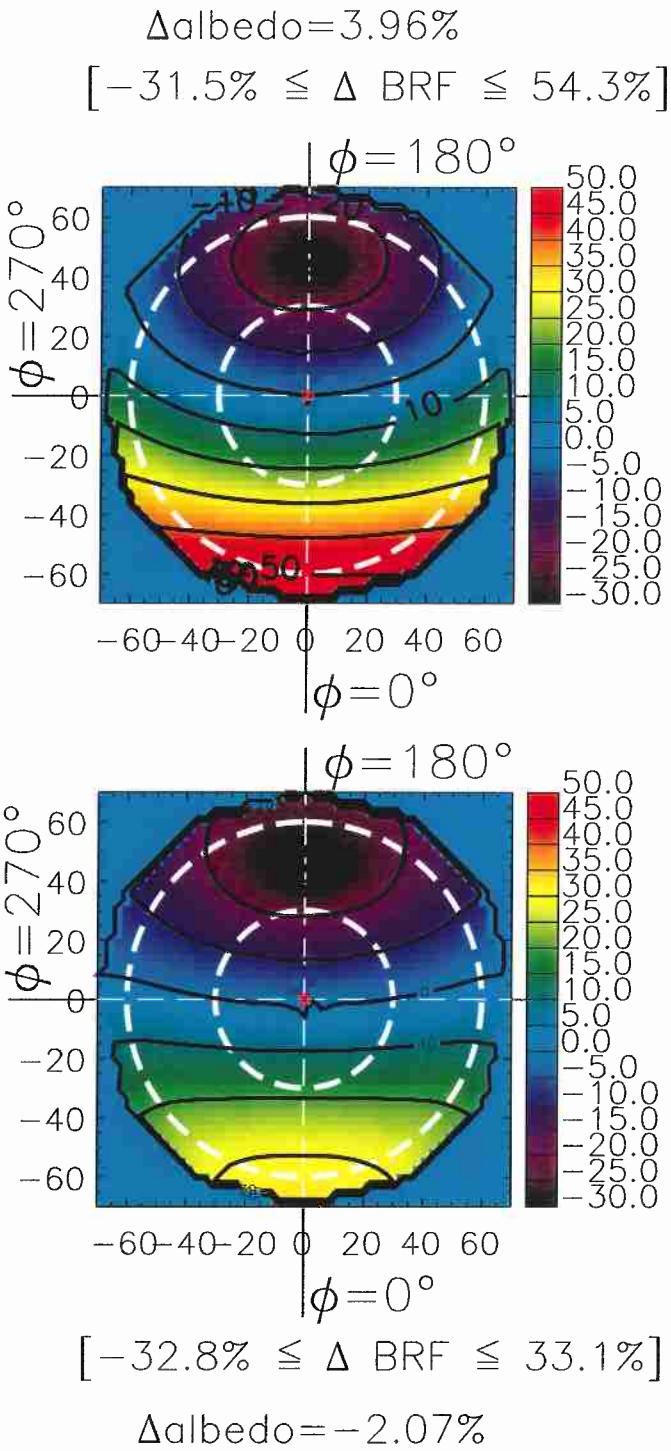

Figure 2.14: Case 9: Directional BRF and hemispherical albedo retrieval accuracy in percent when using the nadir observation only and the Lambertian assumption in the RED (top) and NIR (bottom). Further details as in figure 2.12

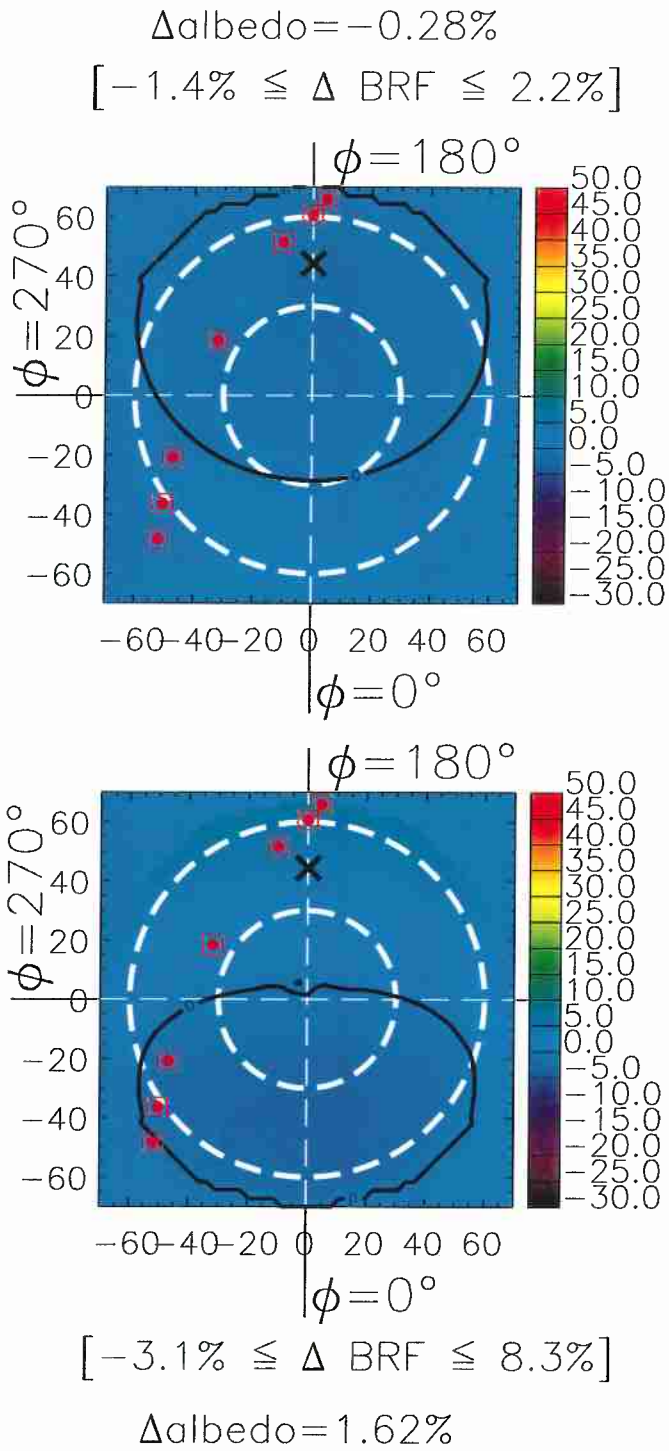

Figure 2.15: Case 12: Directional BRF and hemispherical albedo retrieval accuracy in percent when using the 7 PRISM angles of observation for a simulated orbit over the IMGRASS test site in the red (top) and NIR (bottom). Further details as in figure 2.9

Case 9:
As for Case 8, only the nadir observation is used to reconstruct the BRF field. This permits the direct comparison between the assumption of a typical BRF field (Case 8) and the Lambertian surface reflectance (Case 9) on the retrieval accuracy of the BRF field as well as the albedo. Due to the Lambertian assumption, the nadir BRF is assigned to the entire BRF field. As a result, the typical bowl-shape of the BRF field cannot be represented. The higher reflectance in the backscattering region is underestimated and the lower reflectance in the forward scattering region overestimated. Measurements along the cross plane show the smallest deviation, since here the anisotropy of the surface is the least pronounced. Compared to Case 8, the BRF error range is twice the size with 90% in the RED spectral band and 60% in the NIR. In general, the BRF field is better represented in Case 8 than in Case 9. For observation zenith angles $\theta < 60°$ in the NIR, the Lambertian assumption results in BRF deviation of up to 60% (+30% to −30%), while the assumption of the typical BRF field yields only up to 20% deviations. The results of Case 8 and Case 9 indicate that the retrieval accuracy of the BRF field can be improved by approximately 50% by assuming a typical BRDF shape instead of implying the Lambertian assumption.

Under Lambertian assumptions, the BRF directly corresponds to the albedo. The albedo retrieval accuracy in Case 9 is therefore strongly dependent on the solar position. For example, if the Sun as well as the observer are at nadir, the local reflectance maximum of the hotspot is observed and the Lambertian assumption results in an overestimation of the albedo (see also figure 2.7 on page 14). Depending on the direction of observation, the integration of the Lambertian (constant) BRF field might coincidently yield the correct albedo value (see figure 2.10 on page 19). The Lambertian assumption results in albedo values which are dependent on the observer direction. However, it is clear that the albedo of the surface should not depend on the observation direction and that the assumption of a typical BRF field will yield such a result. The higher albedo deviations in Case 8 compared to Case 9 should therefore not be misunderstood in the sense that the Lambertian assumption is better to derive the albedo. The accuracy in albedo retrieval for Cases 8 and 9 is strongly dependent on the direction of illumination and observation.

Case 12:
Case 12 investigates the retrieval performance under realistic measurement conditions. The GMV simulated orbit 3, for the time period 15-29 of March over the IMGRASS test site, has been selected to study the impact of a near-nadir observation (see figure 2.4). All seven nominal PRISM observation angles are used in the orbit simulation. The resulting polar plot (figure 2.15, page 25) displays the relative azimuth by opposition to the absolute azimuth as provided by GMV in figure 2.4 on page 8. The

retrieval accuracy for both the BRF field and the albedo is comparable to the results in Case 3 (figure 2.12). These results further confirm the potential usefulness of the additional information contained in multiple directional observations, which should be utilized to derive the BRF field, the albedo, and biophysical parameters in a more precise way.

In a similar fashion, Case 12 is applied in the Appendix (page 33) for all surface types listed in table 2.1 and a solar zenith angle of $\theta_0 = 20°, 50°$.

2.7 Atmospheric impacts

One of the major goals of the LSPIM mission is the derivation of surface properties, such as the BRF field and the surface albedo. In operational mode, the PRISM sensor will obtain data at the TOA level, which incorporate atmospheric effects. The proper 'removal' of these effects is a pre-requisite for any further interpretation of the surface reflectance field and its derivatives. The aim of this section is to document the impact of different atmospheric conditions on the TOA reflectance field and to investigate the capability of the PRISM sensor to adequately capture this field.

Various atmospheric conditions are investigated over the reconstructed Aspen BRF field (figure 2.1) in the RED and NIR spectral domains. They are parameterized using the 6S-model (Vermote et al.[29]) and three aerosol types (continental, maritime, urban), five aerosol optical depths $(0.00, 0.05, 0.10, 0.20, 0.4$ at 550 nm), a mid-latitude summer atmosphere, and a solar zenith angle of $\theta_0 = 50°$ (figure 2.16 on page 28). The BRFs are depicted along the plane with the relative azimuth $\phi = 30°, 210°$. Vertical lines denote the PRISM directions of observation and the black solid curve shows the BRF profile without atmosphere at the surface.

For an aerosol optical depth of $\delta = 0.0$ there is obviously no dependence on the aerosol type. In this case, only Rayleigh scattering is present, and its effects is more pronounced at shorter wavelengths ($\propto \lambda^{-4}$). In the NIR it can almost be neglected and the TOA BRF field is close to the surface BRF field (solid line). In the RED channel, the Rayleigh scattering increases the BRF at TOA level, particularly for high off-nadir observations due to the increased atmospheric path length. The introduction of an increasing amount of aerosol over a dark background (RED spectral domain, top of figure 2.16) mainly affects the atmospheric backscattering of direct sunlight to the sensor. In addition, the very strong increase of the scattering phase function for phase angles $g > 90°$ causes the TOA BRF to increase more in the forward than the backward scattering region. Here, the magnitude of this increase reflects the different absorption features of the aerosol types under investigation. For example, the urban aerosol exhibits the minimum increase due to the strong absorption induced by the soot particles. For all cases, the resulting TOA BRF field shows a ra-

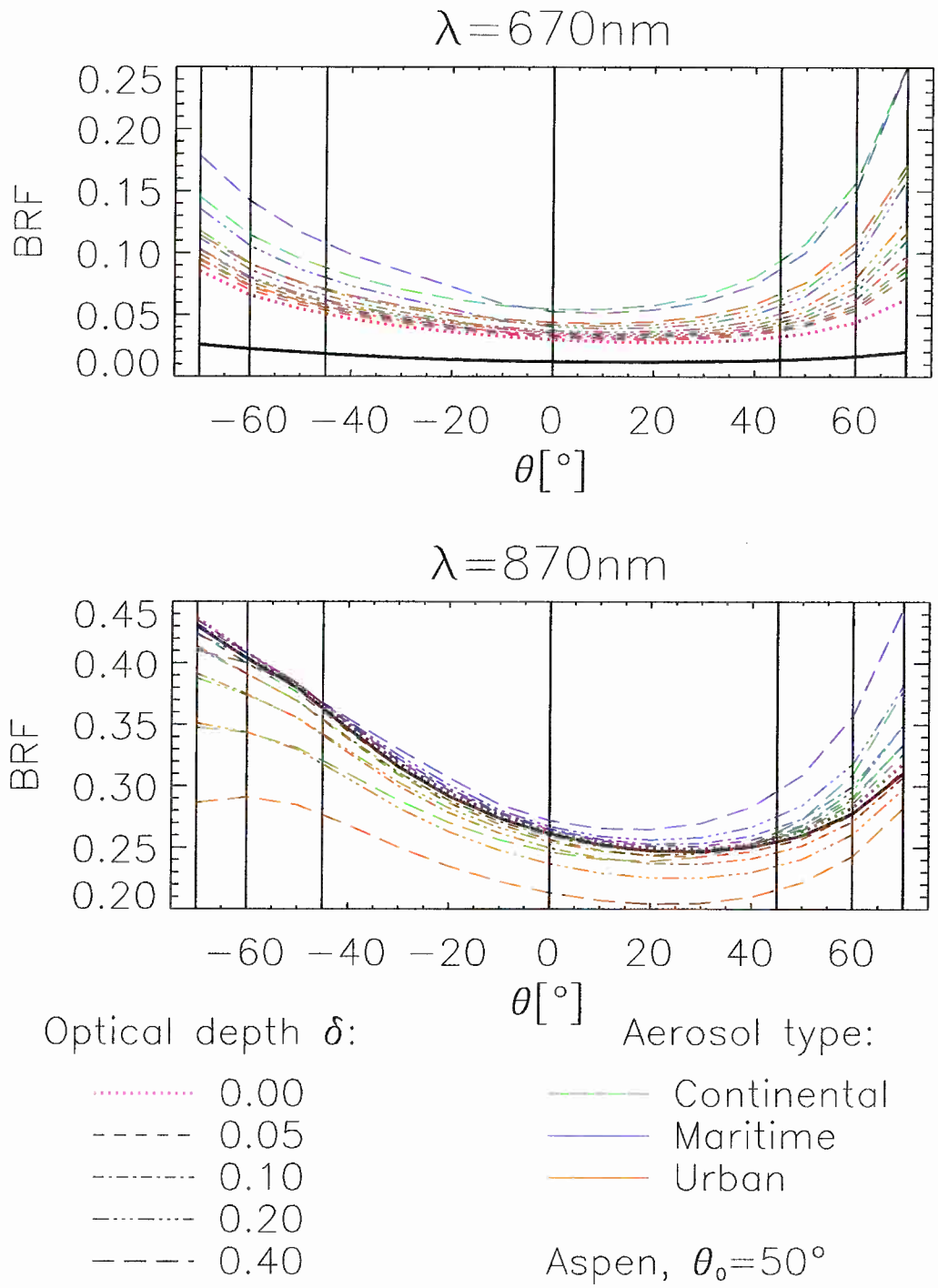

Figure 2.16: Impact of different atmospheric conditions (simulated with the 6S code) in the RED (top) and NIR (bottom) on the TOA BRFs along the azimuthal plane $\phi = 30°, 210°$. The vertical lines indicate the PRISM angles of observation and the bold solid line the surface BRFs.

ther more pronounced bowl shape than the corresponding surface BRF field. In the NIR, the bright surface reflectance intensifies the multiple scattering processes between the atmosphere and the underlying ground. As a consequence, the atmospheric absorption features have a decreasing effect on the TOA reflectance field. This is most pronounced for the urban aerosol, leading to a decreased TOA BRF when compared to the surface BRF. Only in the forward scattering region the strongly increased phase function prevails over the effects of absorption and results in a net increase of the TOA BRF.

For both wavelengths, the TOA BRF field has a different shape and, especially in the RED, magnitude than the surface BRF field. The strongest differences between surface and TOA BRF are found for off-nadir observations for which $\theta > \pm 50°$.

Chapter 3

Conclusions

This report examines the potential increase in albedo and BRF field retrieval accuracy by means of multi-directional measurements. The investigation is applied to the PRISM sensor of ESA's Land-Surface Processes and Interactions Mission (LSPIM). However, the findings of the simulation studies performed in this report could be relevant for other multi-directional instruments like MISR or POLDER. The document is organized in three parts: albedo retrieval accuracy, BRF field retrieval accuracy, and atmospheric impacts on the TOA reflectance field, each in the RED and the NIR spectral domain.

1. *Albedo retrieval accuracy*
   The results of the simulation study of this report can be summarized in two parts:

   - *If several directions of observation are available:*
     Estimations of the retrieval accuracy for albedo are obtained as a function of the number of observations and their location in angular space (Cases 1 through 7, Case 12). The results are as follows: First, a decrease in the number of available observations causes a worse description of the BRF field and, as a consequence, a less accurate albedo retrieval (figure 2.8, page 16). Second, given a fixed number of observations, e.g. 3, it is advantageous to distribute the observations such that they capture as much as possible the bulk of the anisotropic signal.
     The simulated orbit (Case 12) resembles a measurement sequence in the operational mode with a closest to nadir measurement at $\theta > 30°$ instead of the exact nadir observation as simulated in the comparable Case 3, where the observations are along the azimuthal plane $[30°, 210°]$. Nevertheless, the resulting retrieval accuracy for the BRF field and the albedo is similar for both cases. Note that these results are only valid for the single noise distribution considered here. A more reliable statement is achieved by a statistical analysis which requires a repetition of this experiment for a large number of noise fields. Here, the

accuracy of the retrieved BRF field is to be expected to be very close to the 5% noise applied initially.

- *If only one direction of observation is available:*
  The derivation of the albedo is often performed in conjunction with the assumption of a Lambertian surface reflectance. Since no surface shows a Lambertian reflectance behavior, a typical BRDF shape can be defined and the BRF field, as well as the albedo, can be derived using an analytical expression (equation 2.7). Depending on the illumination/observation geometry, the application of the Lambertian assumption (Case 10, page 18) shows an underestimation of up to 35% and an overestimation of up to 55% for the albedo in the RED as well as the NIR spectral bands. The same investigation, using the predefined BRDF shape (Case 11, page 19), results in approximately half the error range due to the consideration of the anisotropic reflectance field. Although, strictly speaking, these findings are valid for the investigated target only, it is straightforward that qualitatively similar results can be expected for other surface types, depending on their degree of anisotropy. However, since every surface exhibits an anisotropic reflectance field, the assumption of a 'typical' BRF field is superior to the one of a Lambertian surface reflectance.

2. *BRF field retrieval accuracy*
   A simulation study is performed using all seven PRISM angles along the azimuthal plane $[30°, 210°]$ (Case 3, figure 2.12 and the figures 3.1 to 3.18 in the Appendix, page 33), a simulated orbital over pass (Case 12, figure 2.15), and a single nadir observation in conjunction with the assumption of a typical BRF field (Case 8, figure 2.13) or a Lambertian surface reflectance (Case 9, figure 2.14).

   In all cases with seven observations, the deviation from the true spectral BRF was at most $\pm 5\%$ for observation angles ($\theta = \pm 60°$). Some higher deviations are found outside this range, however, the deviation in spectral albedo in most cases is found to be less than $\pm 1\%$. When only the nadir observation is used, the assumption of the predefined BRDF-shape again decreased the relative error range of the retrieved BRFs by 50% when compared to the Lambertian assumption.

3. *Atmospheric impacts on the TOA BRF field*
   The precise determination of the surface BRF field requires the consideration and thus characterization of the overlying atmosphere. Simulations are performed with different aerosol types and aerosol loads. They showed major differences between surface and TOA BRF field for observation angles $\theta > \pm 40°$. The PRISM angles of observation permit an adequate sampling of the highly anisotropic

TOA BRF field (figure 2.16) and are therefore appropriate to accurately retrieve the atmospheric properties and to study their impact on the surface BRF fields.

These findings confirm that multiple directional measurements, as provided by the PRISM sensor, will improve the retrieval accuracy for the BRF field and, as a consequence, the albedo. Moreover, the BRF field is strongly related to structural parameters of the vegetation canopy such as the Leaf Angle Distribution (LADF), the Leaf Area Index (LAI), and the gap distribution, which describe the heterogeneity of the surface under study. The improved BRF field derivation may therefore permit a better assessment of surface structural parameters.

The present pre-launch phase of the LSPIM mission is characterized by exploratory research and further simulation studies must be performed on different surface types and the optimization of the observation geometry. In addition, sensor hardware related issues like signal to noise ratio, filter function, pointing accuracy, band to band registration, calibration and stability, sensor Point Spread Function, polarization effects, transient response, etc. need to be addressed. The assessment of the interaction of all components and their joint impact on the retrieval accuracy of the albedo and the BRF field offers a challenging future research field.

Acknowledgments

I gratefully acknowledge the 1-year Marie-Curie Research fellowship of the European Commission, and the authorization of Raytheon ITSS to perform this research at the Space Applications Institute of the Joint Research Centre of the European Commission, Ispra, Italy.

Appendix

The figures on the following pages show the retrieval accuracy of the BRF field and the albedo in the RED and NIR spectral domain for the Case 3, all 9 surface types as outlined in table 2.1 and a solar zenith of $\theta_0 = 20°, 50°$.

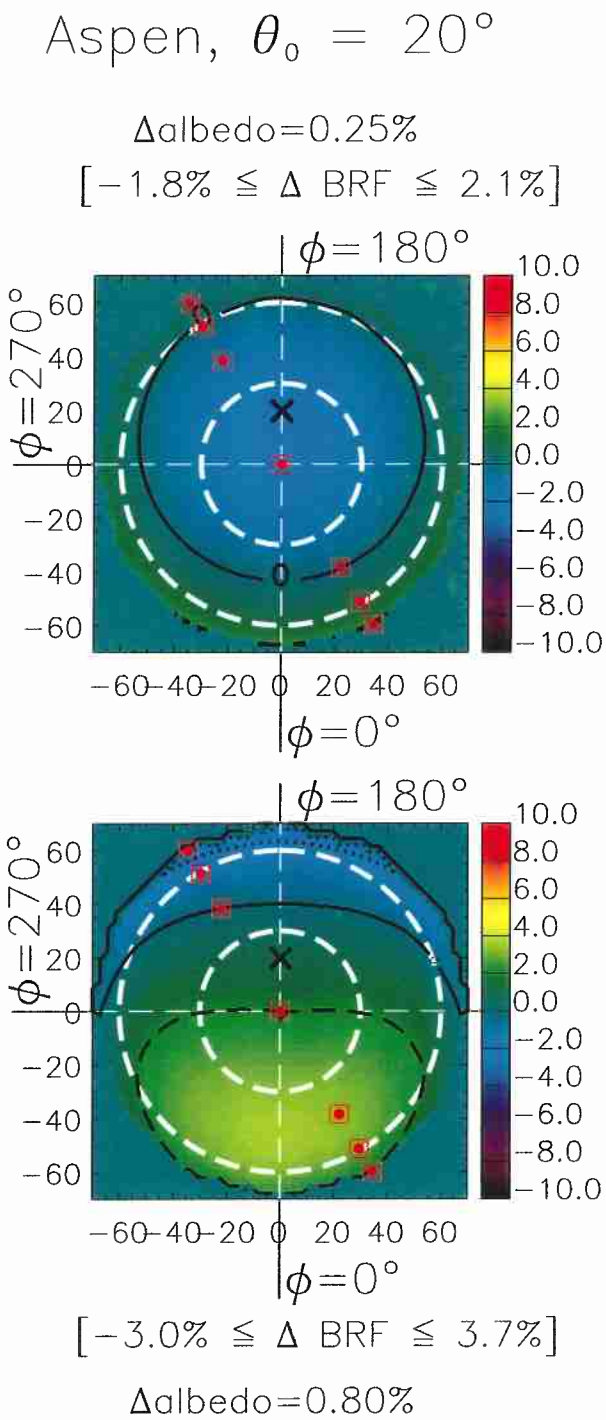

Figure 3.1: Retrieval accuracy in percent of the BRF field and the hemispherical albedo derived from directional BRF measurements (red squared dot) in the RED (top) and NIR (bottom). The surface type is Aspen with a solar zenith of $\theta_0 = 20°$ (cross). The black iso-lines refer to the the BRF retrieval error distribution with a step size of $\Delta 2\%$. Overestimation is denoted by dashed lines, underestimation by dotted lines, and correct retrieval by the solid line. The white dashed circles indicate the observer zenith angle at 30° and 60°. The minimum and maximum BRF deviation is given in brackets. These results are based on an analysis of noisy data, as described on page 6.

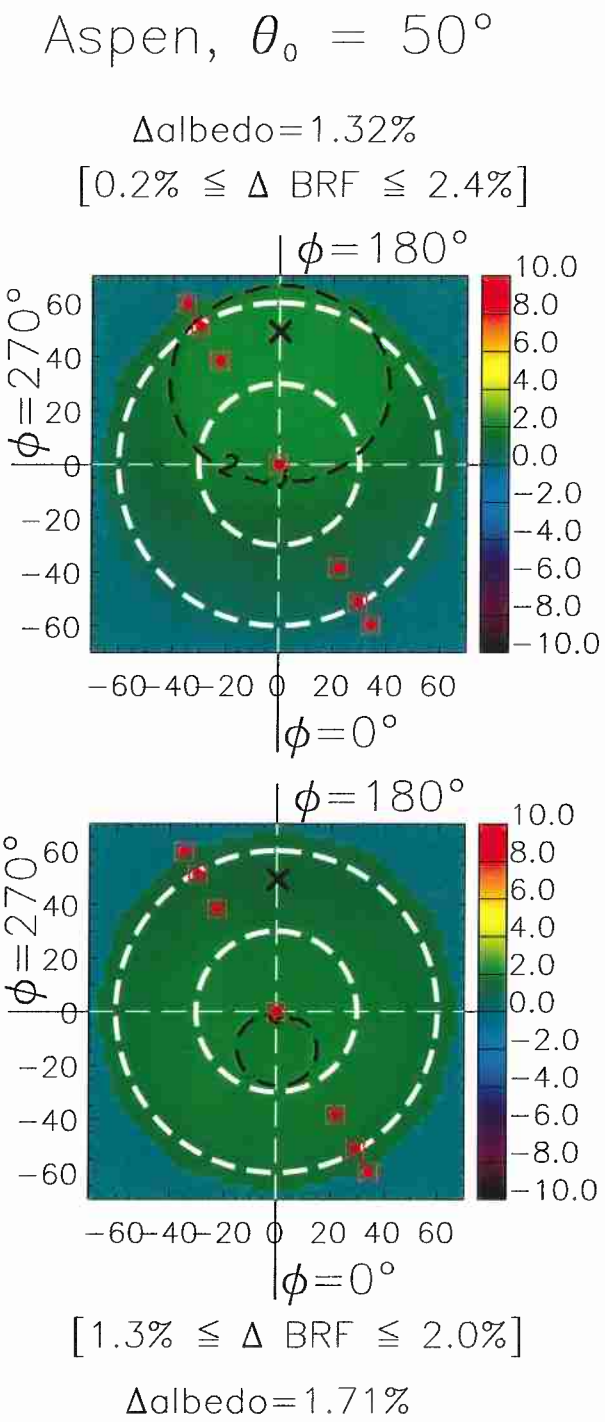

Figure 3.2: Same as figure 3.1 for the surface type Aspen with a solar zenith of $\theta_0 = 50°$ (cross).

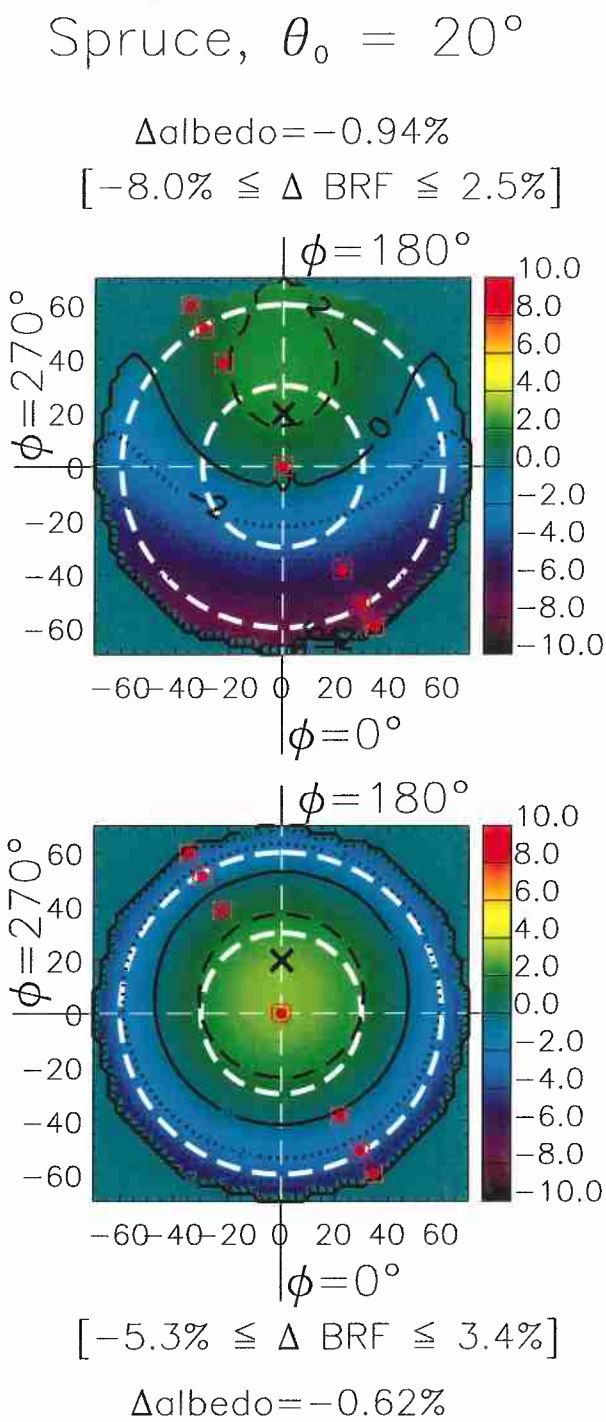

Figure 3.3: Same as figure 3.1 for the surface type Spruce with a solar zenith of $\theta_0 = 20°$ (cross).

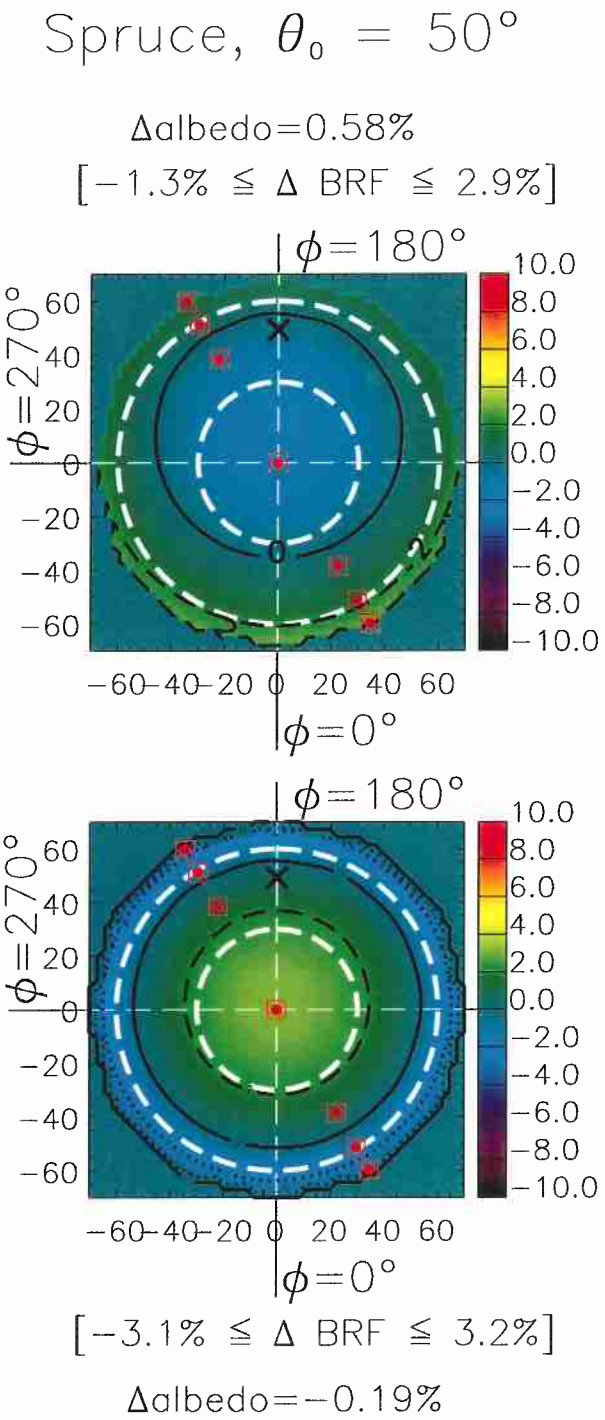

Figure 3.4: Same as figure 3.1 for the surface type Spruce with a solar zenith of $\theta_0 = 50°$ (cross).

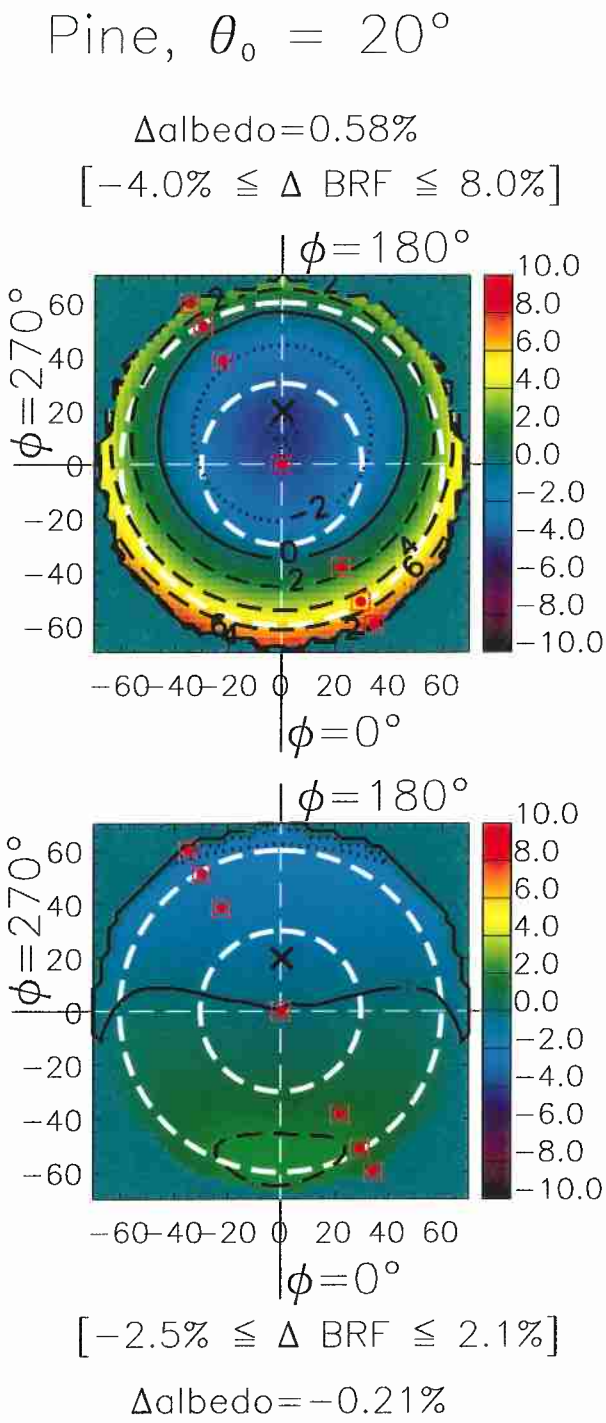

Figure 3.5: Same as figure 3.1 for the surface type Pine with a solar zenith of $\theta_0 = 20°$ (cross).

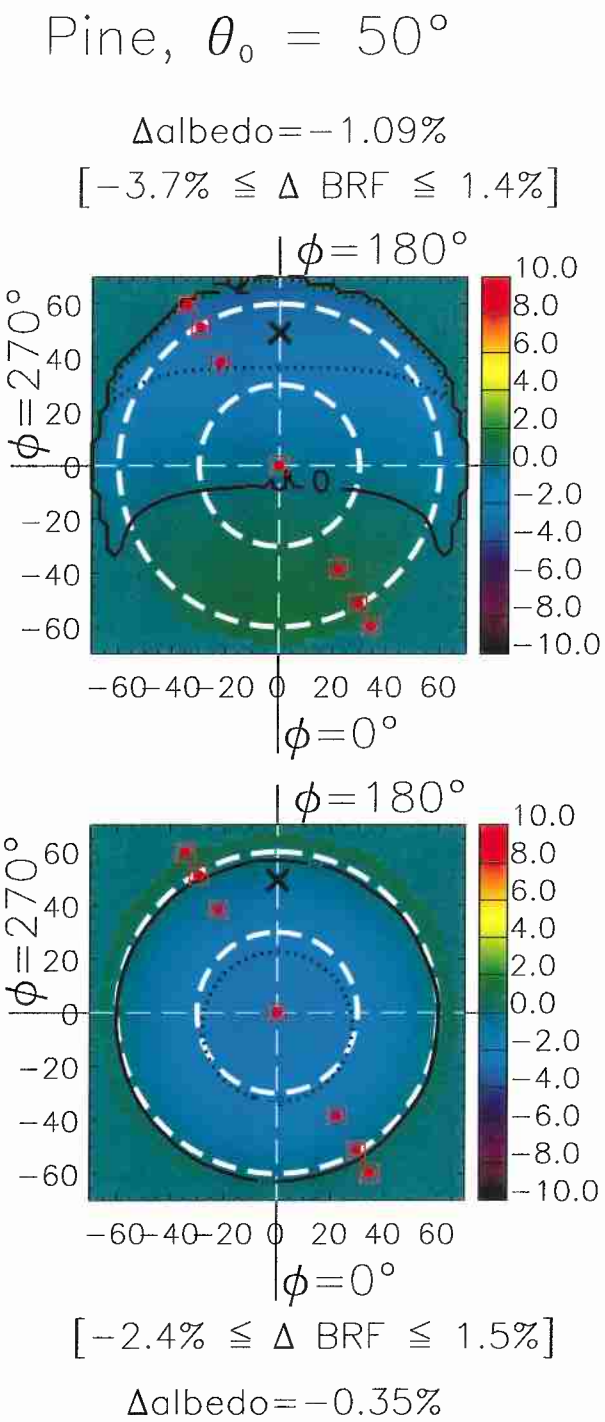

Figure 3.6: Same as figure 3.1 for the surface type Pine with a solar zenith of $\theta_0 = 50°$ (cross).

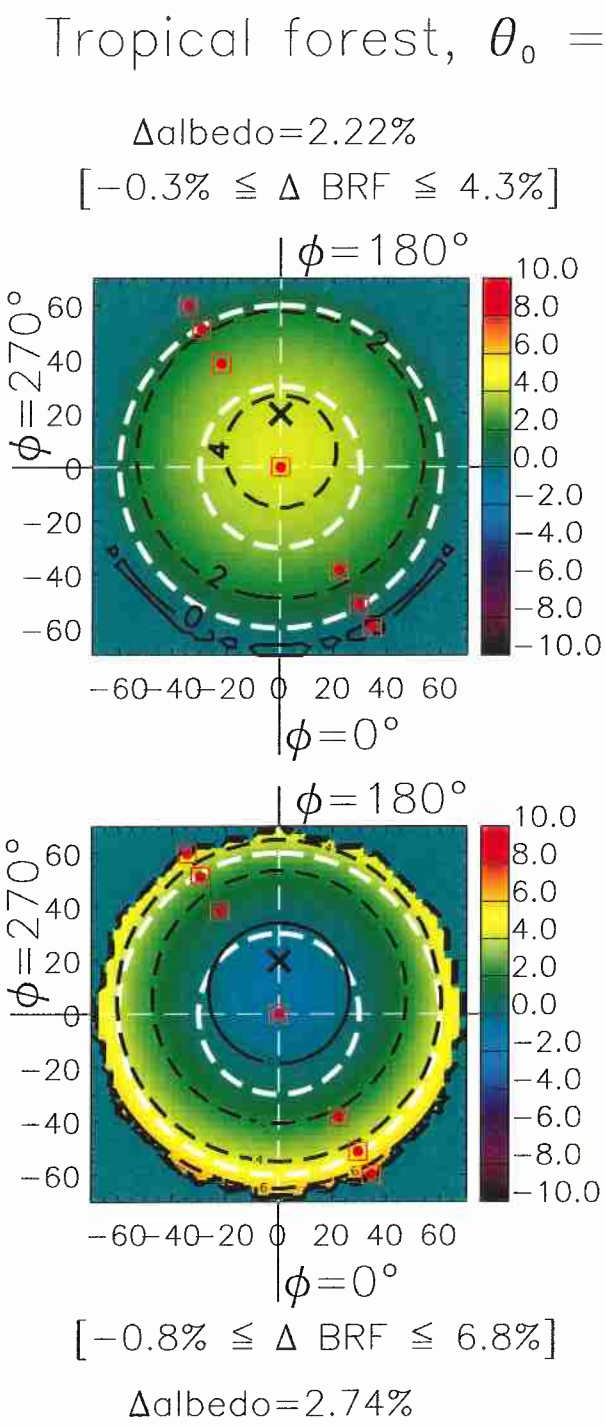

Figure 3.7: Same as figure 3.1 for the surface type Tropical forest with a solar zenith of $\theta_0 = 20°$ (cross).

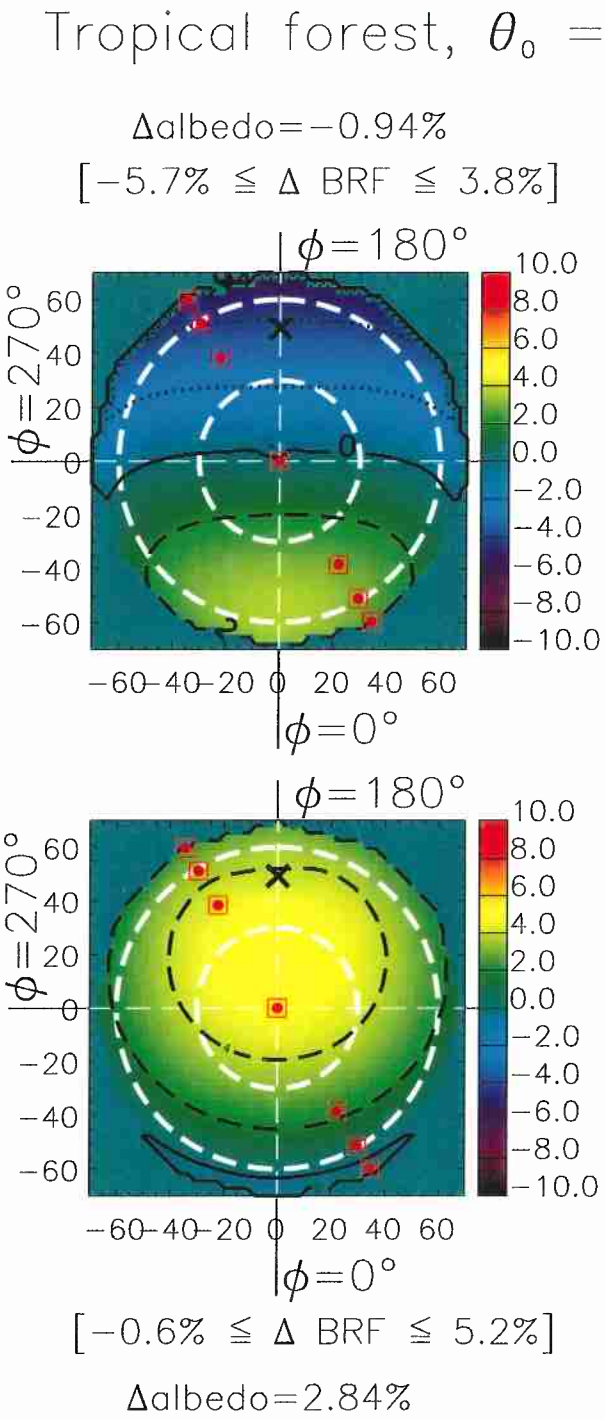

Figure 3.8: Same as figure 3.1 for the surface type Tropical forest with a solar zenith of $\theta_0 = 50°$ (cross).

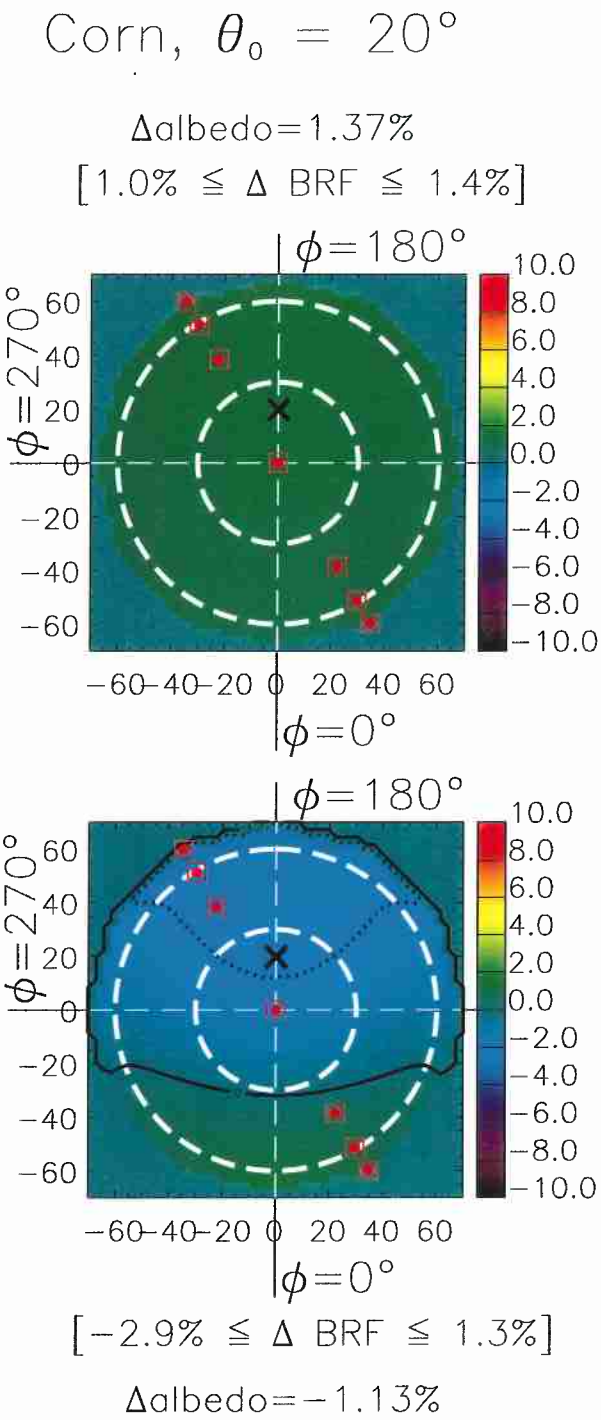

Figure 3.9: Same as figure 3.1 for the surface type Corn with a solar zenith of $\theta_0 = 20°$ (cross).

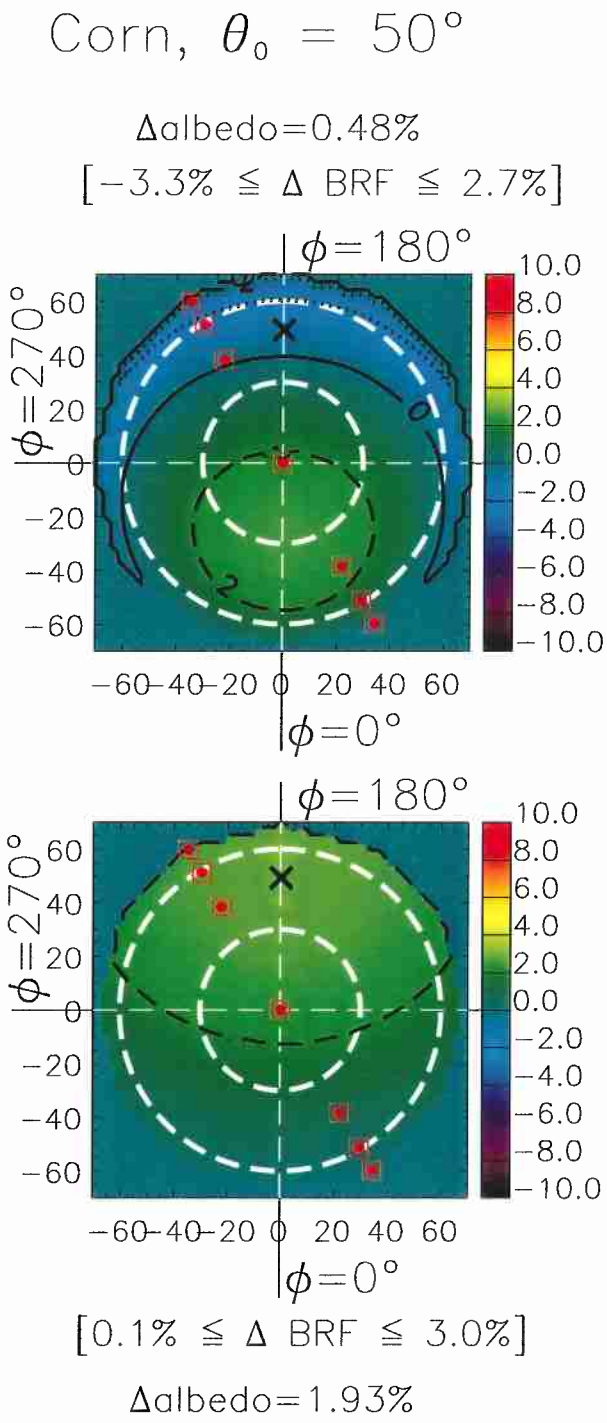

Figure 3.10: Same as figure 3.1 for the surface type Corn with a solar zenith of $\theta_0 = 50°$ (cross).

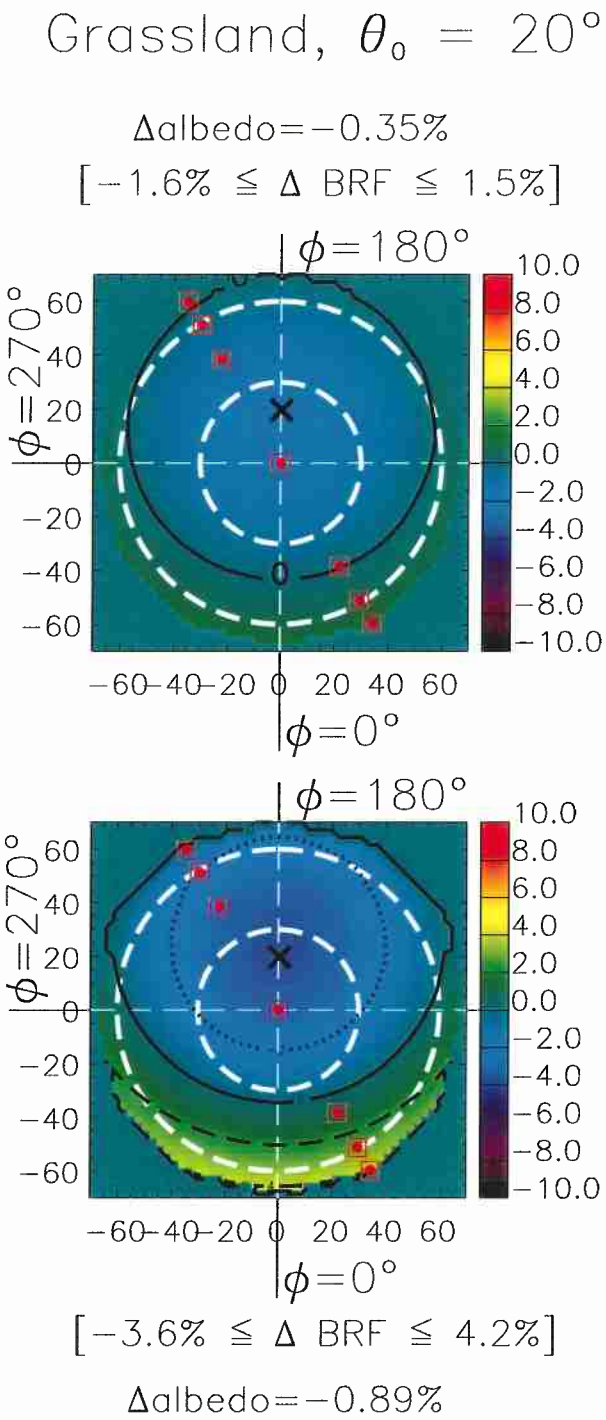

Figure 3.11: Same as figure 3.1 for the surface type Grassland with a solar zenith of $\theta_0 = 20°$ (cross).

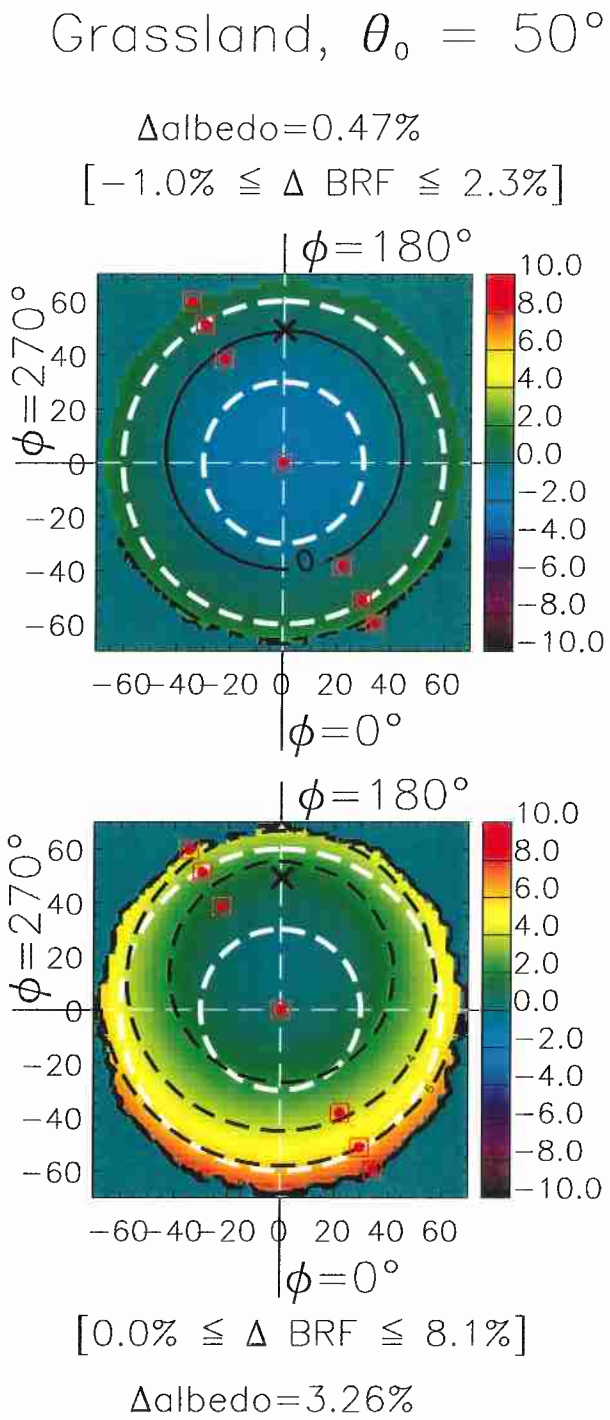

Figure 3.12: Same as figure 3.1 for the surface type Grassland with a solar zenith of $\theta_0 = 50°$ (cross).

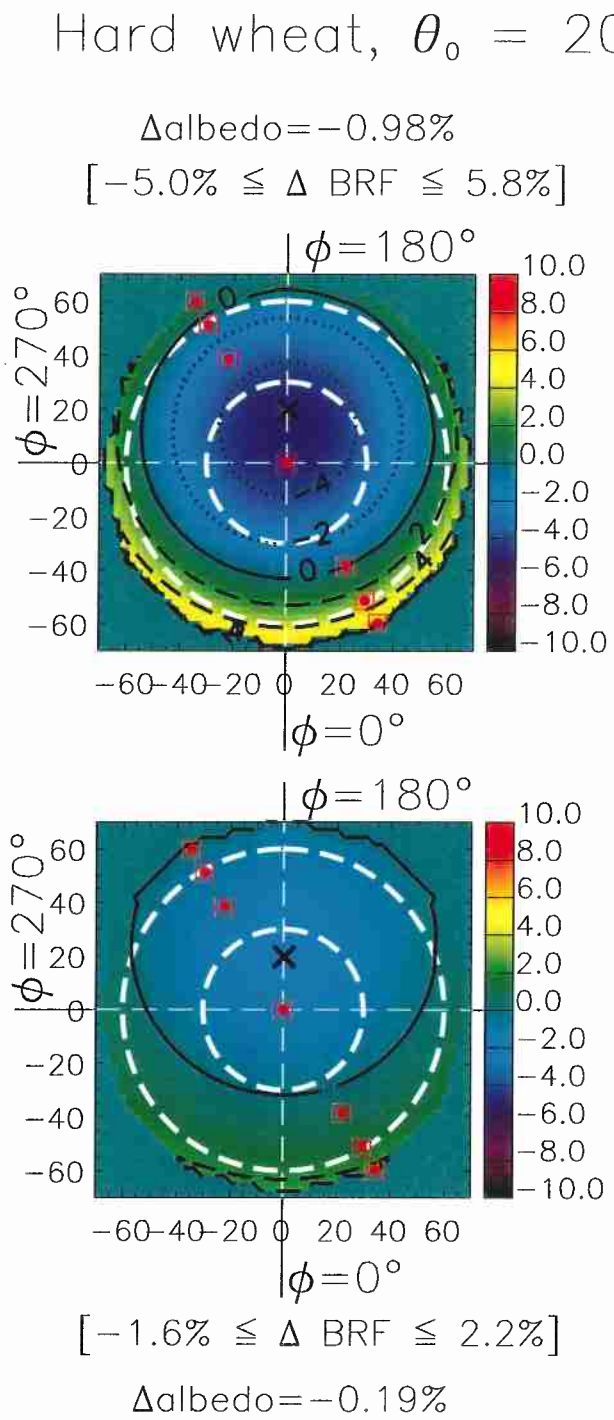

Figure 3.13: Same as figure 3.1 for the surface type Hard wheat with a solar zenith of $\theta_0 = 20°$ (cross).

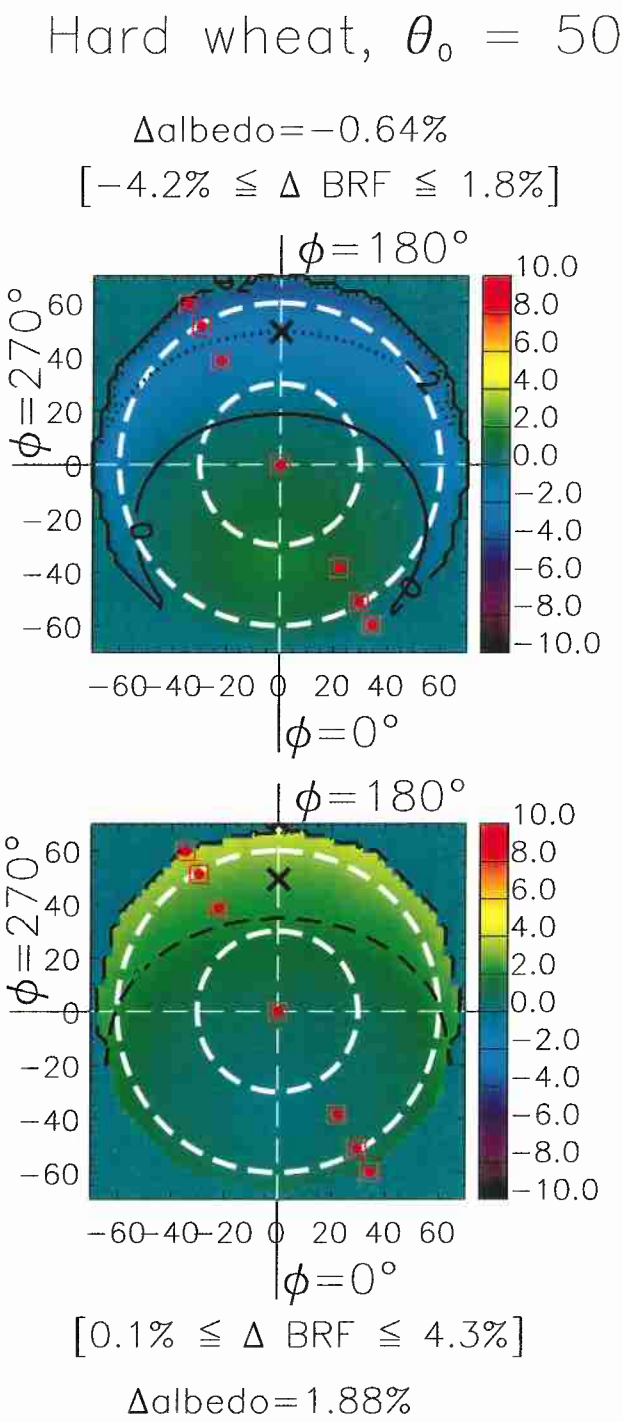

Figure 3.14: Same as figure 3.1 for the surface type Hard wheat with a solar zenith of $\theta_0 = 50°$ (cross).

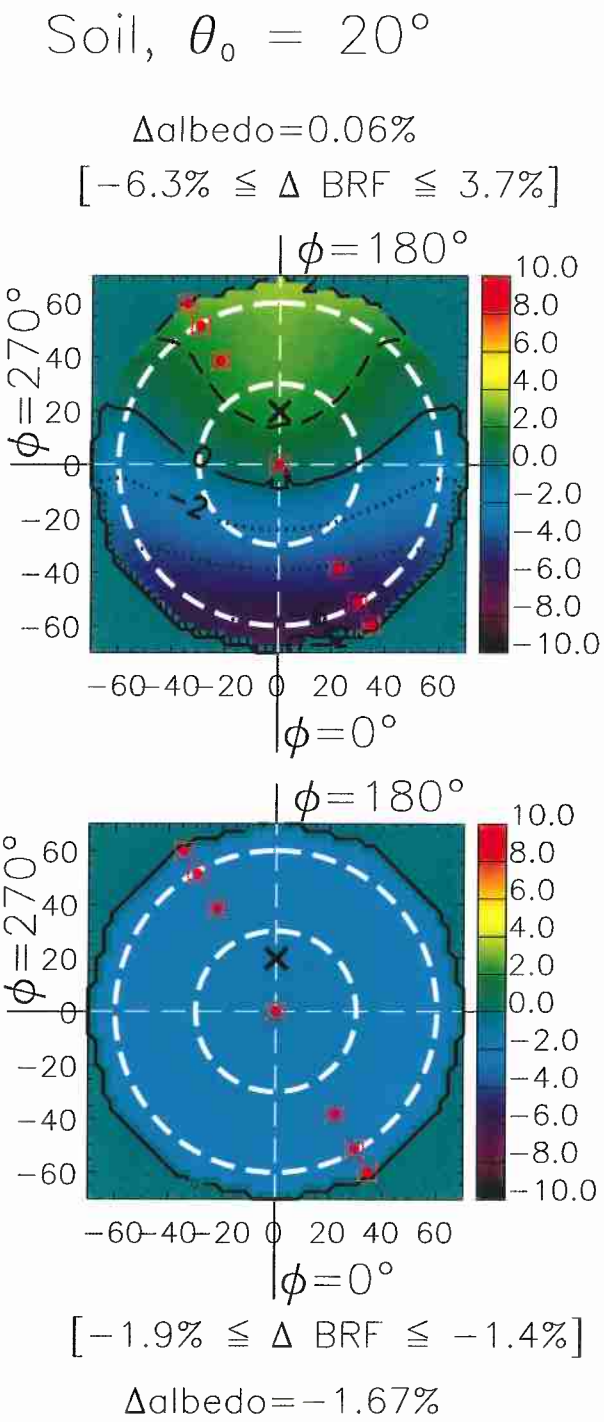

Figure 3.15: Same as figure 3.1 for the surface type Soil with a solar zenith of $\theta_0 = 20°$ (cross).

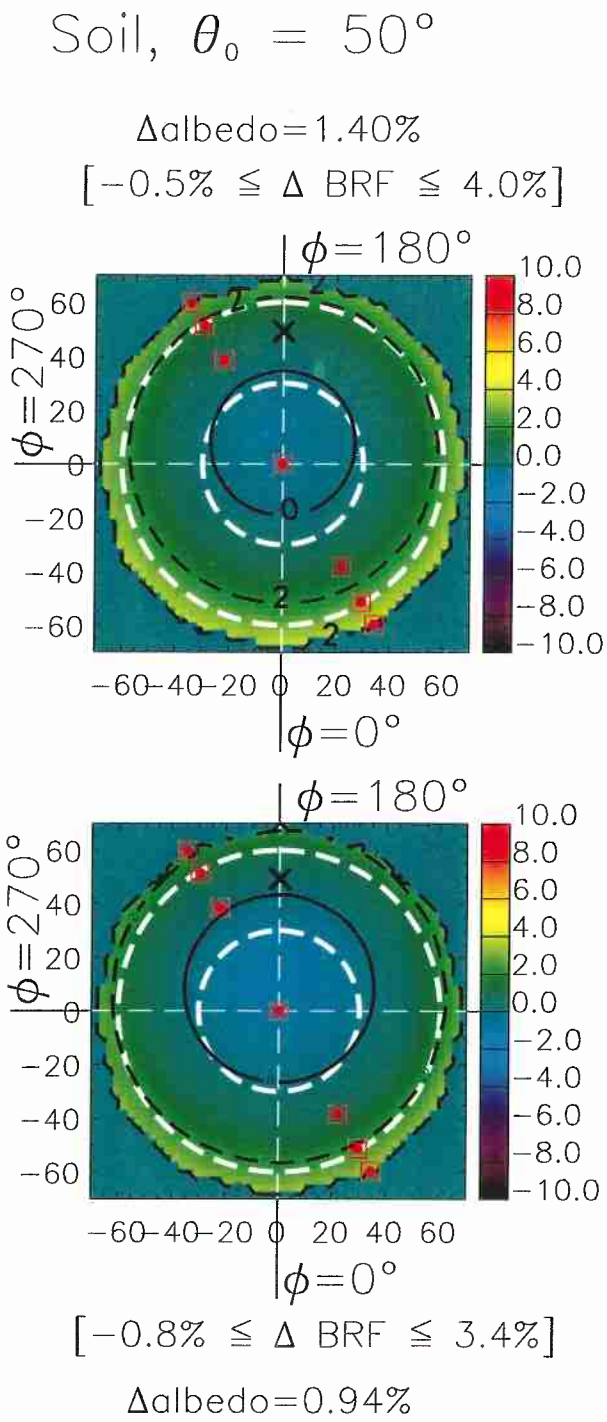

Figure 3.16: Same as figure 3.1 for the surface type Soil with a solar zenith of $\theta_0 = 50°$ (cross).

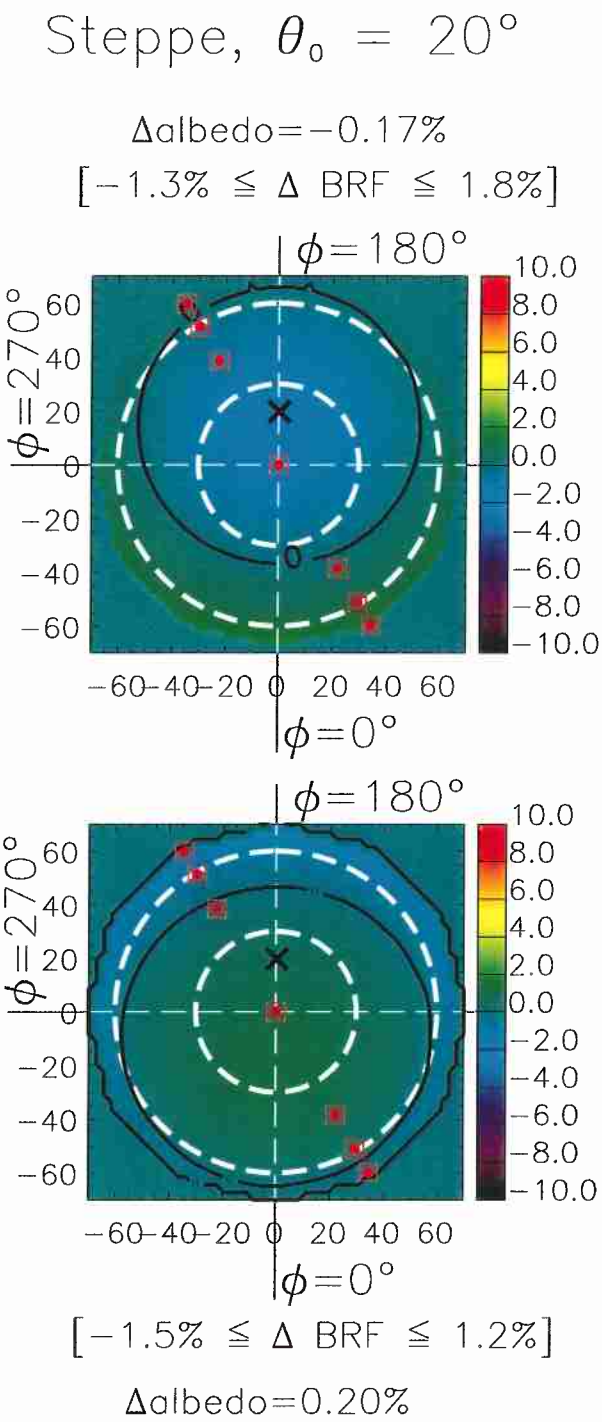

Figure 3.17: Same as figure 3.1 for the surface type Steppe with a solar zenith of $\theta_0 = 20°$ (cross).

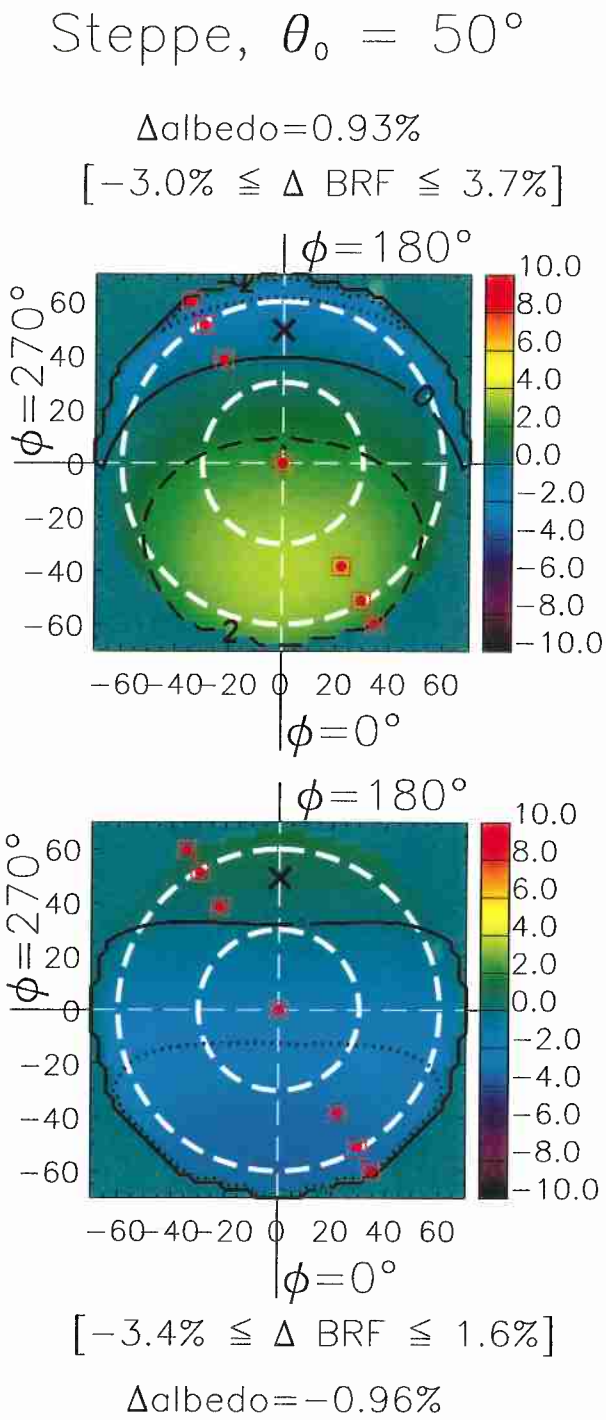

Figure 3.18: Same as figure 3.1 for the surface type Steppe with a solar zenith of $\theta_0 = 50°$ (cross).

Bibliography

[1] Clevers, J.G.P.W. and Büker, C. and van Leeuwen, H.J.C. and Bouman, B.A.M. A Framework for Monitoring Crop Growth by Combining Directional and Spectral Remote Sensing Information. *Remote Sensing of Environment*, 50:161–170, 1994.

[2] Deering, D.W. and Ahmad, S.P. and Eck, T.F. and Banerjee, B.P. Temporal Attributes of the Bidirectional Reflectance for Three Boreal Forest Canopies. In *IGARSS'95*, pages 1239–1241. IEEE Transactions on Geoscience and Remote Sensing, 1995. Florence, Italy.

[3] Deering, D.W. and Leone, P. A shere-scanning radiometer for rapid directional measurements of sky and ground radiance. *Remote Sensing of Environment*, 19:1–24, 1986.

[4] Diner, D. and Abdou, W. and Ackerman, T. and Crean, K. and Gordon, H. and Kahn, R. and Martonchick, J. and Paradise, S. and Pinty, B. and Verstraete, M. and Wang, M. and West, R. ATBD-MISR-09 MISR: Aerosol Retrieval. http://eospso.gsfc.nasa.gov/atbd/misrtables.html, 1997.

[5] Diner, D. and Davies, R. and DiGirolamo, L. and Moroney, C. and Muller, J.P. and Paradise, S. and Wenkert, D. and Zong, J. ATBD-MISR-07 MISR: Level 2 Cloud Detection and Classification. http://eospso.gsfc.nasa.gov/atbd/misrtables.html, 1996.

[6] Engelsen, O. and Pinty, B. and Verstraete, M.M. and Martonchik, J.V. Parametric Bidirectional Reflectance Factor Models: Evaluation, Improvements and Applications. ECSC–EC–EAEC Brussels · Luxembourg Catalogue: CL–NA–16426–EN–C, European Commission, JRC, IRSA, Ispra, Italy, 1996. European Commission, Directorate General XII, L–2920 Luxembourg.

[7] F.E. Nicodemus and J.C. Richmond and J.J. Hsia and I.W. Ginsberg and T. Limperis. Geometrical Considerations and Nomenclature for Reflectance. Technical report, National Bureau of Standards, Dept. of Commerce, Washington, D.C., 1977. NBS Monograph 160.

[8] Gerstl, S.A.W. and Gebauer, W. and Borel, C.C. and Dochitoiu, C. Angular Signature Retrieval and Comparison with Spectral Signa-

tures from AirMISR Data. In *IGARSS'99*. IEEE Transactions on Geoscience and Remote Sensing, 1999. Hamburg, Germany.

[9] Irons, J.R. and Campbell, G.S. and Norman, J.M. and Graham, D.W. and Kovalick, W.M. Prediction and Measurement of Soil Bidirectional Reflectance. *IEEE Transactions on Geoscience and Remote Sensing*, 30(2):249–260, 1992.

[10] Irons, J.R. and Ranson, K.J. and Williams, D.L. and Irish, R.R. and Huegel, F.G. An off-nadir pointing imaging spectroradiometer for terrestrial ecosystem studies. *IEEE Transactions on Geoscience and Remote Sensing*, 29:66–74, 1991.

[11] Kahn, R. and West, R. and McDonald, D. and Rheingans, B. Sensitivity of multiangle remote sensing observations to aerosol sphericity. *Journal of Geophysical Research*, 102:16861–16870, 1997.

[12] Kimes, D.S. Dynamics of directional reflectance factor distribution for vegetation canopies. *Applied Optics*, 22:1364–1372, 1983.

[13] Kimes, D.S. and Newcomb, W.W. Directional scattering properties of a wintering deciduous hardwood canopy. *IEEE Transactions on Geoscience and Remote Sensing*, GE(25):510–515, 1987.

[14] Kimes, D.S. and Newcomb, W.W. and Nelson, R.F and Schutt, J.B. Directional Reflectance Distributions of a Hardwood and Pine Forest Canopy. *IEEE Transactions on Geoscience and Remote Sensing*, GE-23:695–704, 1986.

[15] Kimes, D.S. and Newcomb, W.W. and Tucker, C. and Zonneveld, I. and Van Wijngaarden, W. and de Leeuw, J. and Epema, G. Directional reflectance factor distributions for cover types of northern Africa in NOAA 7/8 AVHRR Bands 1 and 2. *Remote Sensing of Environment*, 18:1–19, 1985.

[16] Kimes, D.S. and Sellers, P.J. Inferring hemispherical reflectance of the Earth's surface for global energy budgets from remotely sensed nadir or directional radiance values. *Remote Sensing of Environment*, 18:205, 1985.

[17] Kriebel, K.T. The spectral reflectance of a vegetated surface (in German). *Contributions to Atmospheric Physics*, 47:14–44, 1974.

[18] Kriebel, K.T. *Reflection Properties of Vegetated Surfaces: Tables of Measured Spectral Biconical Reflectance Factors.* Münchener Universitäts-Schriften, Fachbereich Physik, Nr. 29, 1977.

[19] Kriebel, K.T. Measured spectral bidirectional reflection properties of four vegetated surfaces. *Applied Optics*, 17:253–259, 1978.

[20] Leroy, M. and Deuze, J.L. and Bréon, F.M. and Hautecoeur, O. and Herman, M. and Buriez, J.C. and Tanré, D. and Bouffies, S. and Chazette, P. and Roujean, J.-L. Retrieval of atmospheric properties and surface bidirectional reflectances over land from POLDER/ADEOS. *Journal of Geophysical Research*, 102(14):17023–17037, 1997.

[21] Martonchik, J.V. and Diner, D.J. and Kahn, R.A. and Ackerman, T.P. and Verstraete, M.M. and Pinty, B. and Gordon, H.R. Techniques for the retrieval of aerosol properties over land and ocean using multi-angle imaging. *IEEE Transactions on Geoscience and Remote Sensing*, 36:1212–1227, 1998.

[22] Pinty, B. and Verstraete, M.M. Extracting Information on Surface Properties From Bidirectional Reflectance Measurements. *Journal of Geophysical Research*, 96:2865–2874, 1991.

[23] Rast, M. and LSPIM Committee. Land–Surface Processes and Interactions Mission. Technical Report ESA SP-1233(2), European Space Agency, ESA Publications Division, c/o ESTEC, PO Box 299, 2200 AG Noordwijk, The Netherlands, July 1996. ISBN 92-9092-528-0.

[24] Sellers, P.J. Canopy reflectance, photosynthesis and transpiration II: The Role of Biophysics in the Linearity of Their Interdependence. *Remote Sensing of Environment*, 21:143–183, 1987.

[25] Sellers, P.J. and Berry, J.A. and Collatz, G.J. and Field, C.B. and Hall, F.G. Canopy Reflectance, Photosynthesis, and Transpiration. III. A reanalysis Using Improved Leaf Models and a New Canopy Integration Scheme. *Remote Sensing of Environment*, 42:187–216, 1992.

[26] Shuttleworth, W.J. and Dickinson, R.E. Comments on 'Modelling tropical deforestation: A study of GCM land-surface parametrizations' by R.E. Dickinson and A. Henderson-Sellers (January B 1988, **114**, 439-462. *Quarterly Journal of the Royal Meteorological Society*, 115:1177–1179, 1989.

[27] Sud, Y.C. and Molod, A. A GCM simulation study of the influence of Saharan evapotranspiration and surface-albedoanomalies on July circulation and rainfall. *Monthly Weather Review*, 116:2388–2400, 1988.

[28] Vermote, E. ATBD-MOD-08 MODIS: Atmospheric Correction Algorithm Spectral Reflectances. http://eospso.gsfc.nasa.gov/atbd/modistables.html, 1999.

[29] Vermote, E. and Tanré, D. and Deuzé, J.L. and Herman, M. and Morcrette, J.J. Second Simulation of the Satellite Signal in the So-

lar Spectrum (6S). Technical report, NASA-Goddard Space Flight Center-Code 923, Greenbelt, MD 20771, USA, 1997.

[30] Vogt, P. On the retrieval of the Leaf-Area-Index Using Bi-directional Reflectance Factors in the Near Infrared. In *EOS, Transactions, American Geophysical Union, 1998 Fall Meeting*, volume 79 of *45*, page F262, November 10 1998 / Supplement.

[31] von Schönermark, M. and Vogt, P. and Weimann, A. and Witt, H. Schätzung von Wasserhaushalts- und Pflanzenparametern der Landoberflächen aus Multisensordaten. *DLR–Nachrichten*, 77:19–23, Febr. 1995.

European Commission

EUR 19016 EN - On the Retrieval Accuracy of the Albedo and BRF Fields: Potential of the LSPIM/PRISM-Sensor
Authors: Peter Vogt, Michel M. Verstraete, Bernard Pinty, Massimo Menenti, Augusto Caramagno, Michael Rast
1999–64pp.–21.0x29.7cm
Environment series

Abstract

A parametric BRF model is used to generate a BRF data base for several surface types. In order to approximate actual measurement conditions, these BRFs are artificially contaminated with a realistic amount of noise. The same model which are used in a forward mode to reconstruct the BRF field and to estimate the albedo values. The retrieval accuracy of BRF fields and the albedo is assessed by comparing the original and the corresponding retrieved data sets. The study is applied to the nominal directions of observation provided by the PRISM sensor of ESA's Land-Surface Processes and Interactions Mission. The capability of the PRISM sampling strategy to usefully sample the variance of the top-of-atmosphere BRF field is investigated by simulating different atmospheric conditions over the measured surface BRF field of an Aspen forest.